Hindawi
IET Electrical Systems in Transportation
Volume 2023, Article ID 6658744, 24 pages
https://doi.org/10.1049/2023/6658744

Research Article

Current Ripple Reduction Employing the Reactor of DC–DC Converter to Have Variable Inductance through Magnetic Saturation

Chang-Ho Lee,[1] Tuan-Vu Le,[1] Feel-soon Kang,[2] and Sung-Jun Park[3]

[1]*G&EPS Co. Ltd., Jangseong-gun, Jeollanam-do 57248, Republic of Korea*
[2]*Department of Mechatronics Engineering, Gyeongsang National University, Jinju 52725, Republic of Korea*
[3]*Department of Electrical Engineering, Chonnam National University, Gwangju 61186, Republic of Korea*

Correspondence should be addressed to Feel-soon Kang; feelsoon@gnu.ac.kr

Received 3 June 2023; Revised 26 August 2023; Accepted 15 September 2023; Published 27 October 2023

Academic Editor: I. Safak Bayram

When DC distribution grids with different voltage levels are connected, harmonic currents flow into the grid under light load conditions, which is a significant cause of grid instability. In this paper, we proposed a method to reduce the current ripple at light load by designing a bidirectional DC–DC converter reactor to have an inductance variable according to the load power capacity. The inductance is varied using magnetic saturation and implemented in three ways: two magnetic circuits in one magnetomotive force (MMF) circuit, a single magnetic circuit in one MMF circuit, and two magnetic components with different magnetic permeability in one MMF circuit. The feasibility is verified through simulation and experiments targeting the 750 and 380 V DC grid connection. The operating characteristics and efficiency are compared and analyzed by applying the existing and proposed variable reactor to a bidirectional DC–DC converter.

1. Introduction

Alternating current (AC) distribution networks generate higher power losses than DC distribution networks due to power conversion losses and line resistance during power transmission. In addition, as the policy to expand the proportion of renewable energy generation is implemented worldwide, DC power sources such as photovoltaic power and fuel cells are rapidly increasing, and the importance of DC systems is increasing [1–7]. Accordingly, research on bidirectional DC–DC converters for stable energy transfer according to various DC operating voltages is actively conducted [8–23].

When a switching-type power converter, such as a digital load or an electric vehicle, is connected to a DC-distributed power source, harmonic components adversely affect the system's stability. Many converters installed in the DC distribution system cause harmonic currents to flow into the grid due to high-switching frequency operation, causing malfunction of various equipment. In particular, incoming harmonic currents directly affect the life span and efficiency of batteries for an energy storage system (ESS). In connecting DC distribution systems with different voltage levels, current harmonic components flowing into the system at light loads are the leading cause of instability in the power supply system [24–27]. Harmonic reduction technology for converters is essential. However, most harmonic reduction technologies studied in the microgrid converters are primarily developed for harmonic reduction between the DC distribution system and the DC grid [28–48]. Among them, a technique to reduce ripple by configuring two DC voltages across two capacitors connected with opposite polarities using a buck–boost DC–DC converter has been introduced [30–32]. Since the sum of the ripple energy stored in the two capacitors is approximately equal to the pulsating energy of the system, the pulsating energy does not appear on the DC bus. It can reduce both dc bus voltage ripple and dc bus capacitance [35]. adopts a method of injecting the third harmonic component into the input current to minimize the DC bus capacitor. The reduced pulsating input power reduces the DC bus's ripple power and capacitor volume. Lowering ripple by injecting harmonic

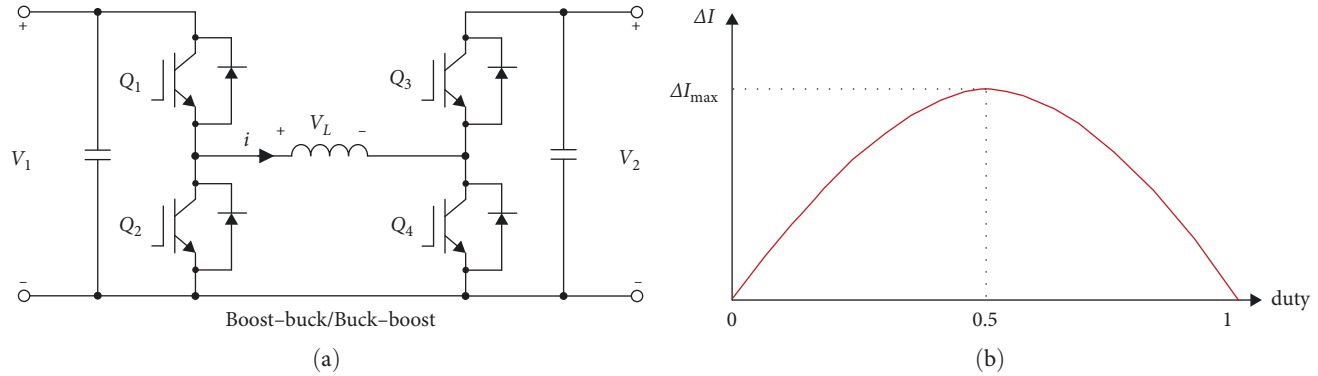

Figure 1: Bidirectional DC–DC converter structure and current ripple according to duty ratio, (a) Converter structure applicable to the DC distribution grids with different voltage levels and (b) current ripple according to the duty ratio [49].

current or distorting the input current changes the amount of energy delivered to the load in each fundamental cycle [36]. This scheme does not add components to the power circuit but has the problem of increasing the input current's total harmonic distortion. A method of adding an energy storage circuit in parallel with the DC bus capacitor to bypass the ripple current flowing through the DC bus capacitor has been introduced [39–42]. By Cao et al. [41], a circuit was constructed with one capacitor, one inductor, and two power switches to absorb and emit ripple energy during different half cycles. Since the ripple current is compensated with an average value instead of an instantaneous value, the voltage ripple is significantly reduced but not satisfactory. A method of connecting an active compensator in series with the dc bus line has been proposed [45, 46]. Since the compensator serves as a voltage source to offset the voltage ripple, the voltage stress of the added compensator decreases due to series operation, but since the ripple power for a specific load is fixed, the current stress of the compensator increases. In particular, only the DC voltage after the compensator is clean with no noticeable low-frequency ripple. However, the DC voltage before the compensator still has a large low-frequency ripple. In a DC microgrid system, there can be a wide variety of widely distributed sources and loads, making it challenging to apply existing methods to all DC sources and loads.

This paper proposes a harmonic reduction technology that can satisfy the same current ripple rate regardless of transmission current to construct a stable power supply system with less harmonic current influence on the DC-distribution grid and dc grid.

This paper's most important technical contribution is a method to reduce the current ripple at light load by designing the reactor of the bidirectional DC–DC converter to have variable inductance through magnetic saturation according to the load power capacity. Three methods are proposed to create a variable reactor: two magnetic circuits in one MMF circuit, one magnetic circuit in one MMF circuit, and two magnetic materials with different magnetic permeability in one MMF circuit. A 750-V DC grid and a 380-V DC grid are configured for simulation and experiment. The operating characteristics and efficiency are analyzed by applying the existing and proposed reactor to the bidirectional DC–DC converter.

2. Bidirectional DC–DC Converters in DC Grids

Several DC–DC converters installed in the dc distribution network perform step-up, step-down, and step-up and down functions according to their roles. Renewable energy generation sources and most connected loads operate intermittently, so the system's stability fluctuates frequently.

The ESS converter that controls the grid voltage and the power receiving converter between the grids are continuously operated. Therefore, the worst condition is where only the ESS converter and the power-receiving converter work in the no-load state. The grid's stability becomes the worst due to voltage hunting due to the inflow of harmonic current. In this case, to improve the grid stability, a converter for ESS and a bidirectional DC–DC converter for receiving power are needed to minimize the inflow of harmonic current.

2.1. Bidirectional DCDC Converter. Figure 1(a) shows a bidirectional DC–DC converter structure applicable to the DC-distribution grids with different voltage levels. In a bidirectional DC–DC converter, the current ripple of the reactor determines the switching frequency, inductance, and operating voltage.

$$\Delta I = \frac{d(1-d)\cdot V_i}{f_s \cdot L}. \tag{1}$$

Regardless of the load current, it is determined only by the duty ratio as given in Equation (1), and the maximum current ripple appears when the duty ratio is 0.5, as shown in Figure 1(b).

When the converter's switching frequency is increased to reduce the current ripple, the switching loss increases rapidly depending on the operating voltage and power capacity. Since there is a limit to increasing the switching frequency, it is a general method to design the ripple factor of the rated current to be 30%–40% by increasing the inductance. However, when only the ESS converter and the power converter at the power receiving stage are operated, the grid's stability severely deteriorates due to the current ripple in the no-load condition.

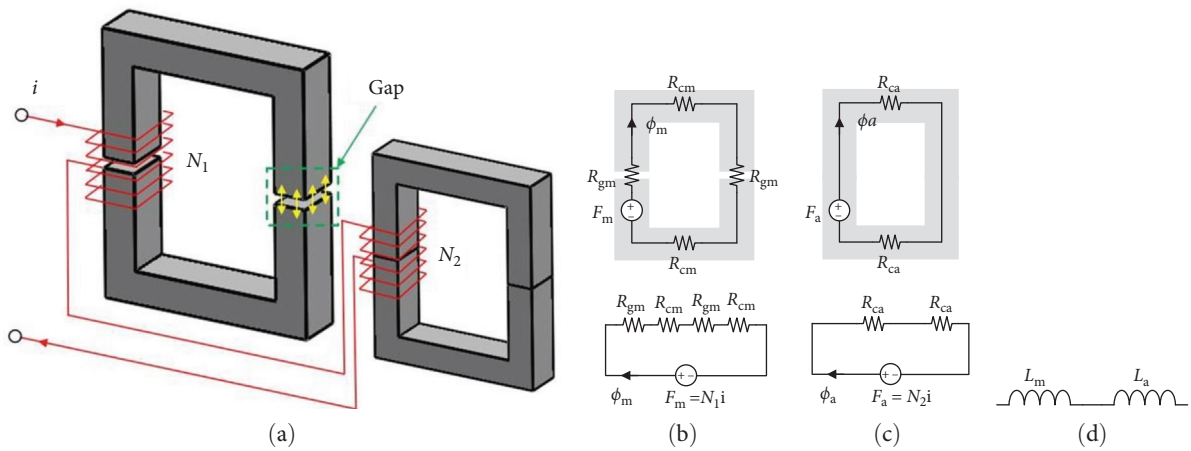

FIGURE 2: The magnetic and electrical equivalent circuit according to two reactor series configuration; (a) series connected reactors with different characteristics, (b) magnetic and electrical equivalent circuit of a reactor with a gap, (c) magnetic and electrical equivalent circuit of a reactor with no gap, and (d) series inductance.

The current ripple of the reactor must be reduced to decrease the harmonic current in standby conditions or light load. The switching frequency or inductance can be changed to lower the reactor current ripple during the light load operation. First, the current ripple can be reduced at light loads by varying the switching frequency according to the load during operation. This method has a limitation due to an increase in switching loss and has a problem in that power conversion efficiency is significantly reduced at light loads. Next, increasing the inductance causes an economic problem due to an increase in the size and weight of the inductor.

To solve this problem, this paper proposes a new type of reactor that can solve economic issues such as the size and weight of the reactors by serially coupling two independent reactors with different characteristics.

2.2. Proposed Concept Composed of Two Independent Reactors in Series. Figure 2 shows an equivalent magnetic and electrical circuit when two independent reactors with different characteristics are connected in series. When a low current flows in a state where a small-value reactor with a large air gap (L_m) and a large-value reactor with a small air gap (L_a) is connected in series, the total inductance appears as the sum of the two inductances. However, when the current increases and the magnetic circuit with the small air gap (L_a) saturates, the total inductance appears only as the inductance with the large air gap (L_m). The relationship between magnetomotive force (MMF), magnetic flux, and inductance without considering the magnetic saturation is as follows:

$$F_m = N_1 I = \left(R_{\text{gm}} + R_{\text{cm}} + R_{\text{gm}} + R_{\text{cm}}\right)\phi_m = R_{\text{eqm}}\phi_m, \tag{2}$$

$$R_{\text{eqm}} = \frac{N_1 I}{\phi_m}, \tag{3}$$

$$L_m = \frac{{N_1}^2}{R_{\text{eqm}}} = \frac{{N_1}^2}{\left(R_{\text{gm}} + R_{\text{cm}} + R_{\text{gm}} + R_{\text{cm}}\right)}, \tag{4}$$

$$F_a = N_2 I = \left(R_{\text{ca}} + R_{\text{ca}}\right)\phi_a = R_{\text{eqa}}\phi_a, \tag{5}$$

$$R_{\text{eqa}} = \frac{N_2 I}{\phi_a}, \tag{6}$$

$$L_a = \frac{{N_2}^2}{R_{\text{eqa}}} = \frac{{N_2}^2}{\left(R_{\text{ca}} + R_{\text{ca}}\right)}. \tag{7}$$

The inductance when the magnetic flux is not saturated is the same as the above formula, but when the magnetic flux is saturated, it becomes zero. The proposed combination of two reactors has a large inductance at a low current where the magnetic flux does not saturate and a small inductance at a large current where the magnetic flux saturates. Therefore, if this reactor is used for a DC–DC converter in a DC–distribution network, it dramatically reduces current ripple at light loads [49].

2.3. Design Consideration of Series-Coupled Reactors with Two Different Characteristics. Figure 3(a) shows the relationship between magnetic flux, current, and inductance according to the air gap in the reactor under the ideal condition. Since the inductance at the rated current (I_{rate}) is determined by the reactor with a large air gap, the inductance considering the current ripple is first calculated under the rated current condition. Next, the inductance of the reactor with a small air gap is computed at a light load considering the current ripple by the reactor with a small air gap.

The inductance value of a reactor with a large air gap that satisfies the current ripple rate at rated current can be obtained from Equation (8)

$$L_m = \frac{d(1-d)\cdot V_i}{f_s \cdot \Delta I_{\text{rate}}}. \tag{8}$$

Here, L_m is the inductance of the reactor with a large air gap, ΔI_{rate} is the ripple factor at rated current, d is the duty

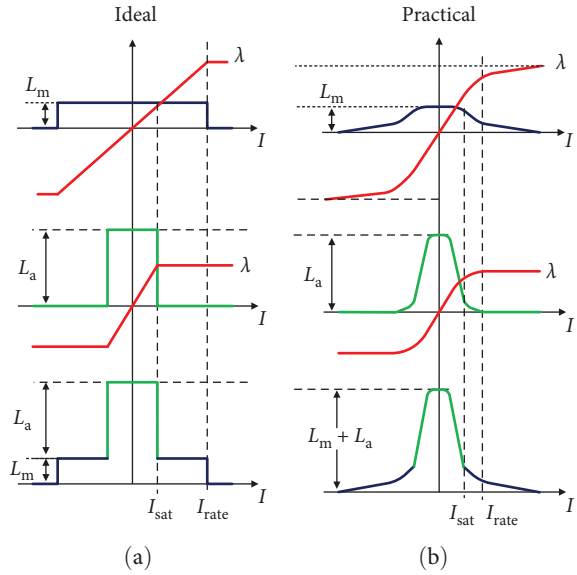

FIGURE 3: Relationship between magnetic flux, current, and inductance for a reactor with a large air gap, a reactor with a small air gap, and the case of connecting the two reactors in series; (a) ideal and (b) practical [49].

ratio, f_s is the switching frequency, and V_i is the input voltage.

The inductance of a reactor with a small air gap that satisfies the current ripple at no load and light load can be obtained from Equation (9)

$$L_a = \frac{d(1-d)\cdot V_i}{f_s \cdot \Delta I_{\text{no-load}}} - L_m. \tag{9}$$

Here, L_a is the inductance of the reactor with a small air gap, $\Delta I_{\text{no-load}}$ is the ripple factor at no load condition, d is the duty ratio, f_s is the switching frequency, and V_i is the input voltage.

Figure 3(b) shows the relationship between magnetic flux, current, and inductance of a reactor in a practical condition. It shows the change of total flux-linkage and inductance according to the current. As the current increases, the magnetic flux density of the core and the total flux linkage become saturated. At this time, the inductance value decreases inversely to the current growth. Even in the practical conditions, when the air gap of the reactor is large, the inductance is small, but the rated current capacity is large.

On the other hand, when the air gap of the reactor is small, the inductance is significant, but the rated current capacity is low. Therefore, by connecting two reactors with different rated current capacities in series, it is possible to design reactors with varying values of inductance depending on the magnitude of the current. The method of varying the inductance value mentioned above is implemented by dividing it into three types, and its characteristics are compared and analyzed. Case 1 configures two magnetic circuits in one MMF circuit. Case 2 is a method implemented by using one magnetic circuit for one MMF circuit. Case 3 is a method of using two magnetic circuits with different permeability in one MMF circuit.

2.3.1. Case 1: Two Magnetic Circuits in One MMF Circuit. Figure 4 shows Case 1, where the inductance is changed by configuring two magnetic circuits in one MMF circuit. Case 1 is constructed using the same magnetic material. A magnetic circuit is built by arranging the distance between the outer and inner magnetic materials to be larger than the air gap [49]. The outside reactor has a large air gap, and the inside reactor has a small air gap. The relationship between MMF and magnetic flux without considering the magnetic saturation phenomenon is as in Equation (10)

$$\phi = \phi_m + \phi_a, \tag{10}$$

where $\phi_m = \frac{\text{NI}}{2\left(R_{\text{cm}}+R_{\text{gm}}\right)}$, $\phi_a = \frac{\text{NI}}{2R_{\text{ca}}}$.

Since the magnetic resistance of the outside reactor is much larger than that of the inside reactor with no air gap, most of the magnetic flux flows into the magnetic circuit by the inside reactor. After the inside magnetic circuit is saturated, most of the magnetic flux is formed in the outside magnetic circuit.

2.3.2. Case 2: Single Magnetic Circuit in One MMF Circuit. Figure 5 shows Case 2, in which the inductance is changed by configuring a single magnetic circuit in one MMF circuit. Case 2 is a method of increasing the air gap by laser cutting on the outer part of the magnetic material. Case 2 uses the same magnetic material so that the outside has a large air gap in the magnetic circuit, and the inside has a small air gap in the single magnetic circuit. The relationship between MMF and magnetic flux without considering magnetic saturation is described in Equation (11)

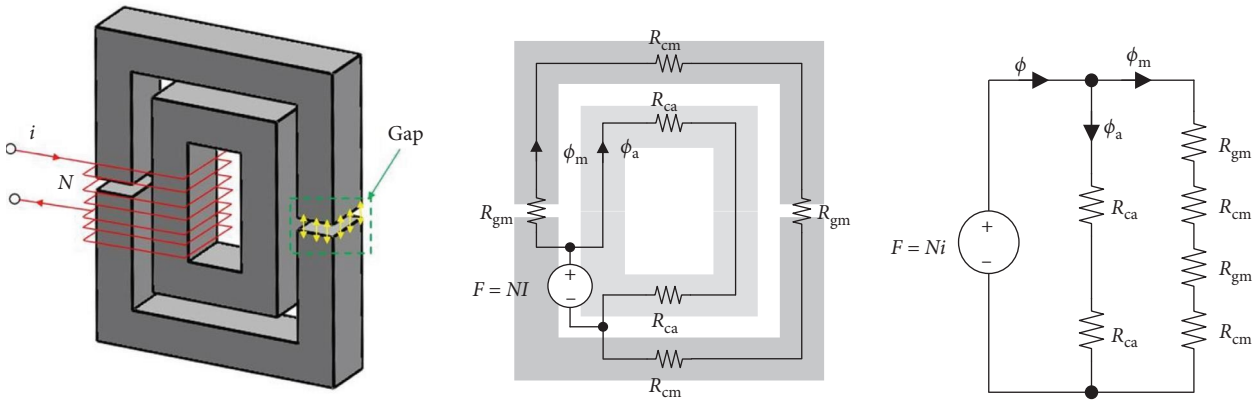

FIGURE 4: A method of varying the inductance by configuring two magnetic circuits in one MMF circuit, (a) Case 1 configuration and (b) equivalent magnetic and electric circuit of Case 1.

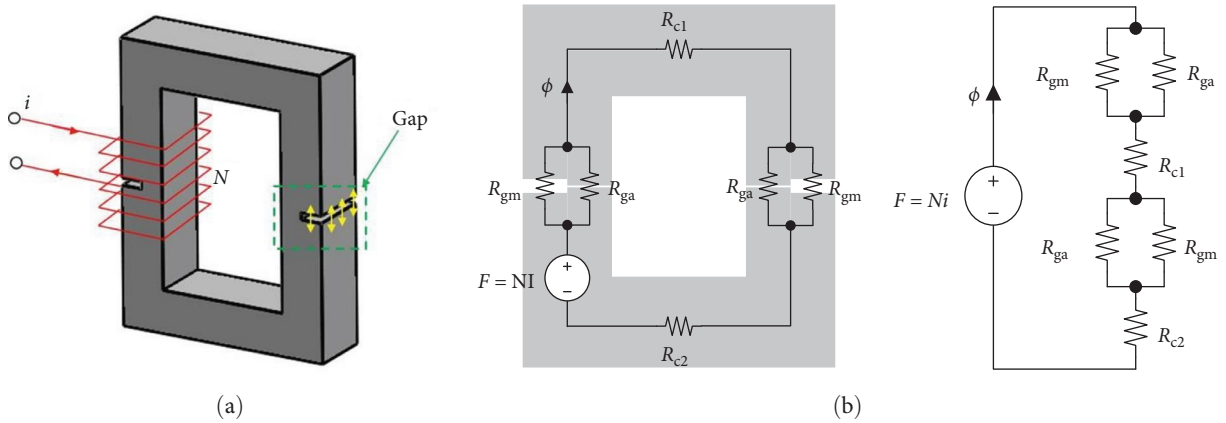

FIGURE 5: A method of varying the inductance by configuring a single magnetic circuit in one MMF circuit, (a) Case 2 configuration and (b) equivalent magnetic and electric circuit of Case 2.

$$\phi = \frac{\mathrm{NI}}{R_{c1} + R_{c2} + 2\left(\frac{R_{ga} \cdot R_{gm}}{R_{ga} + R_{gm}}\right)}. \tag{11}$$

In the structure of Case 2, if the magnetic flux is small, a magnetic path is formed through the inside small air gap. However, magnetic saturation occurs in the inside small air gap when the magnetic flux is large. The equivalent air gap becomes large because magnetic saturation occurs only around the small air gap. At this time, magnetic flux is formed through the large air gap.

2.3.3. Case 3: Magnetic Circuit by Two Magnetic Materials with Different Permeability in One MMF Circuit. Figure 6 shows Case 3, where the inductance can be varied by using a magnetic circuit made of two magnetic materials with different magnetic permeability in one MMF circuit. Case 3 consists of two magnetic materials with different permeability. The outer reactor uses a magnetic material with a small permeability, and the inner reactor uses a very high permeability. The relationship between MMF and magnetic flux without considering magnetic saturation is described in Equation (12)

$$\phi = \phi_m + \phi_a = \left(\frac{R_{ca} + R_{cm}}{R_{ca} \cdot R_{cm}}\right)\mathrm{NI}. \tag{12}$$

Because the inner reactor has a large permeability, the magnetoresistance is smaller than the outer reactor with low permeability. Therefore, most of the magnetic flux flows into the internal magnetic circuit, and after the internal magnetic circuit is saturated, the magnetic flux is formed in the outer magnetic circuit. The magnetic circuit of Case 3 operates as almost independent circuits due to different permeability. It has the effect of significantly reducing the noise of the reactor because there is no air gap.

3. Simulation and Experimental Results

3.1. Simulation Results. Figure 7(a) is a PSIM (Powersim's circuit analysis simulation tool) schematic for simulating the proposed variable reactor concept. Figure 7(b) shows the

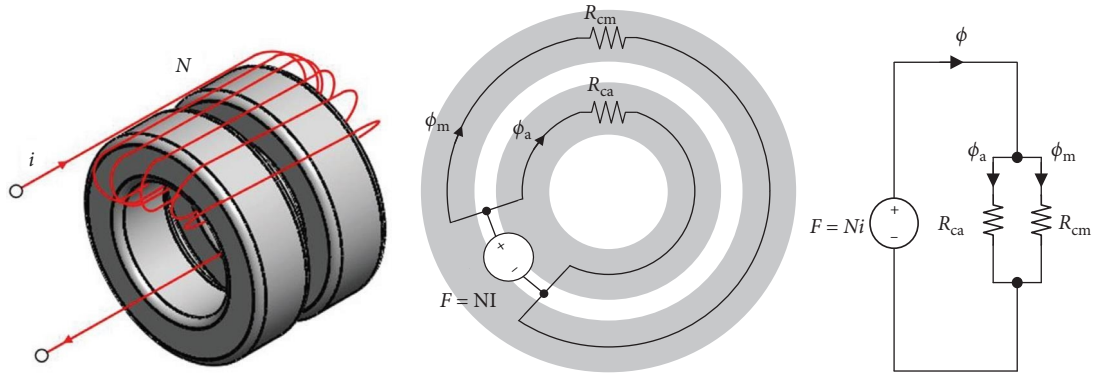

FIGURE 6: A method of varying the inductance by configuring two magnetic materials with different permeability in one MMF circuit, (a) Case 3 configuration and (b) equivalent magnetic and electric circuit of Case 3.

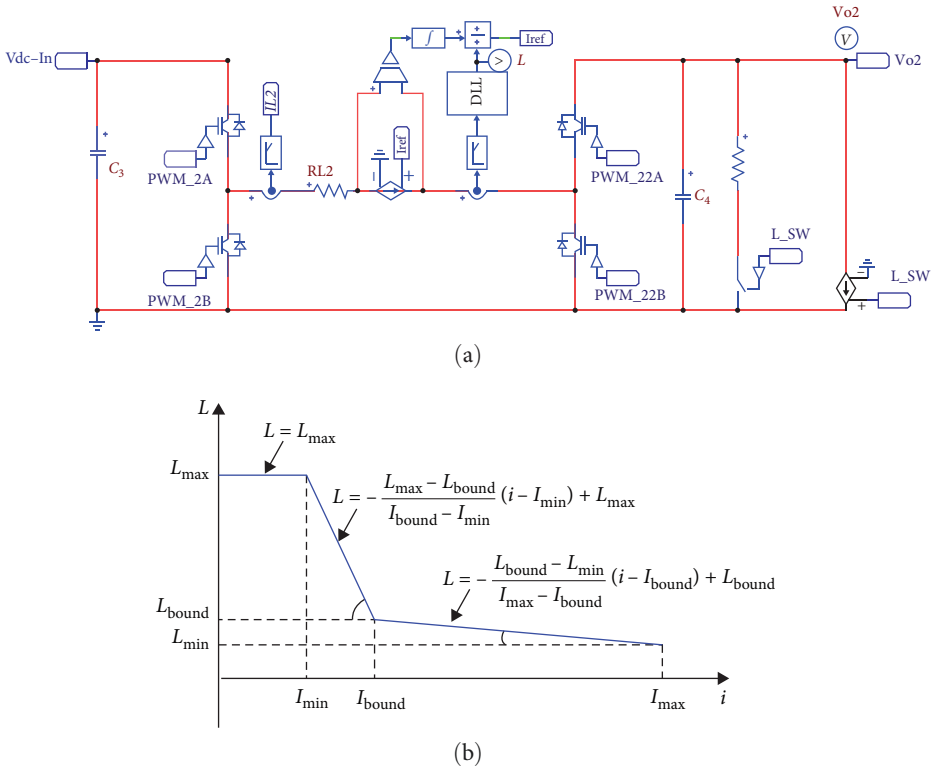

FIGURE 7: Simulation setup,: (a) converter schematic for PSIM simulation and (b) inductance change modeling according to the current magnitude.

slope change of inductance according to the current magnitude to realize variable inductance in simulation. Where L_{max} is the inductance capacity of the reactor with a small air gap (L_a), it starts to saturate at I_{min}. Until I_{bound}, the inductance is modeled as decreasing by L_{a_sat}.

$$L_{a\_sat} = -\frac{L_{max} - L_{bound}}{I_{bound} - I_{min}}(i - I_{min}) + L_{max}. \quad (13)$$

The saturation phenomenon of the reactor with a large air gap (L_m) from I_{bound} to I_{max}, is modeled to have a gentle slope by L_{m_sat}.

$$L_{m\_sat} = -\frac{L_{bound} - L_{min}}{I_{max} - I_{bound}}(i - I_{bound}) + L_{bound}. \quad (14)$$

Table 1 shows the simulation parameters. Although the inductance value decreases nonlinearly when the reactor is saturated, it is modeled linearly to simulate the proposed variable reactor characteristics. Characteristics are analyzed by comparing with a conventional converter with a fixed value reactor under heavy and no-load conditions. In the simulation, the primary inductance (L_m) is simulated with 1.4 mH and the auxiliary inductance (L_a) with 16 mH. Since

Table 1: Simulation parameters.

Parameters	Value	Unit
Inductor		
Conventional	1.4	mH
Inductor		
Large air gap (L_m)	1.4	mH
Small air gap (L_a)	16	mH
Switching frequency	6	kHz
Input voltage	750	V
Output voltage	380	V
Rated power	25	kW
Capacitor		
Input and output	1,000	μF

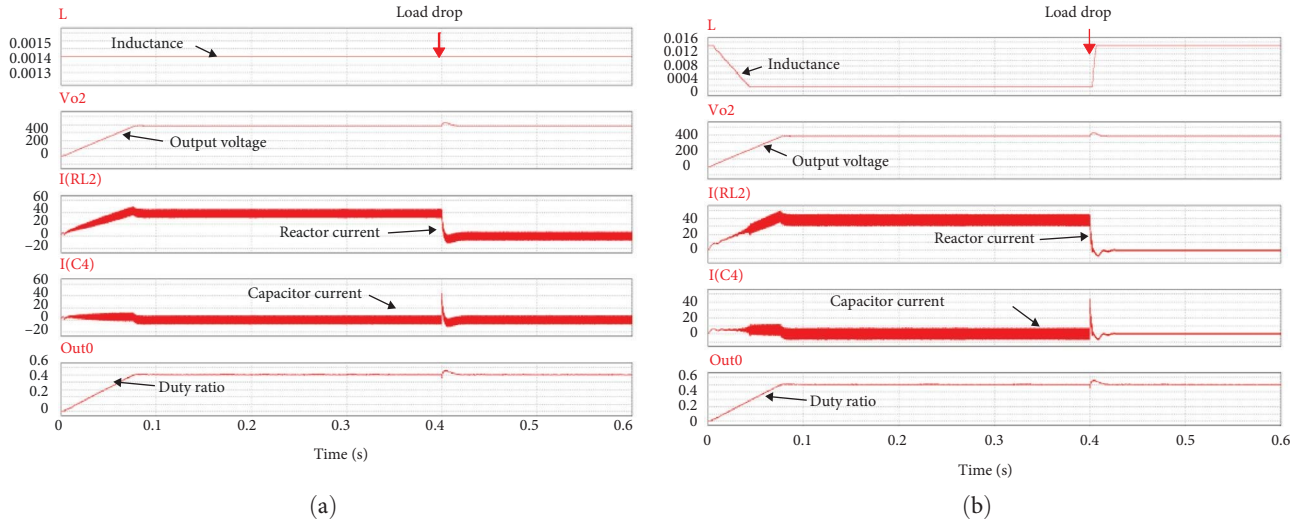

Figure 8: Load drop simulation for voltage control of a bidirectional DC–DC converter; (a) with conventional fixed inductance and (b) with proposed variable inductance.

magnetic saturation could not be implemented as in the experiment, two inductance values (L_m, L_a) with a difference of about 10 times that were suitable for implementing the characteristics of Figure 7(b) were used.

Figure 8 is the load drop simulation for voltage control of a bidirectional DC–DC converter operating with an input voltage of 750 V and an output voltage of 380 V. Figure 8(a) is the simulation result of having a constant inductance of 1.4 mH regardless of the load condition. In this case, the current ripple appears as 17.54 A. The proposed variable reactor in Figure 8(b) is modeled to have an inductance of 1.4 mH under heavy load and an inductance of 16 mH at no load after the load is dropped. It can be seen that the current ripple at no load is significantly lowered to 2.58 A. The initial startup becomes a steady state within 80 ms by applying the soft-start function, and the duty ratio of the steady state becomes 0.529 to control this. When the load is dropped, the output voltage increases to 454 V but returns to a steady state within 18 ms.

Figure 9 shows the reactor current characteristics according to the increase or decrease of the load current when controlling the current of the bidirectional DC–DC converter. The input side is 750 V, and the output side is simulated under 380 V. Figures 9(a) and 9(b) are simulation results when the current command value varies from 30 to 0 A. In both methods, the dynamic characteristics for load fluctuations are almost identical. Since conventional reactors have a fixed inductance, the current ripple is constant regardless of the load. In the case of the proposed variable inductance, since it has 16 mH at no-load and 1.4 mH at heavy load, the current ripple appears close to zero under no-load conditions.

3.2. Prototype Reactor Design

3.2.1. Case 1: Two Magnetic Circuits in One MMF Circuit. Figure 10 shows the design drawing and prototype photo of the reactor to which the Case 1 concept was applied [49]. Case 1 reactor uses UU core composed of the same magnetic material. The air gap of the large core is designed to be 7 mm, the air gap of the small core is 0.1 mm, and the wire is wound with 60 Turns using Litz wire 15SQ. To remove the interference between the large and small cores, the gap between the

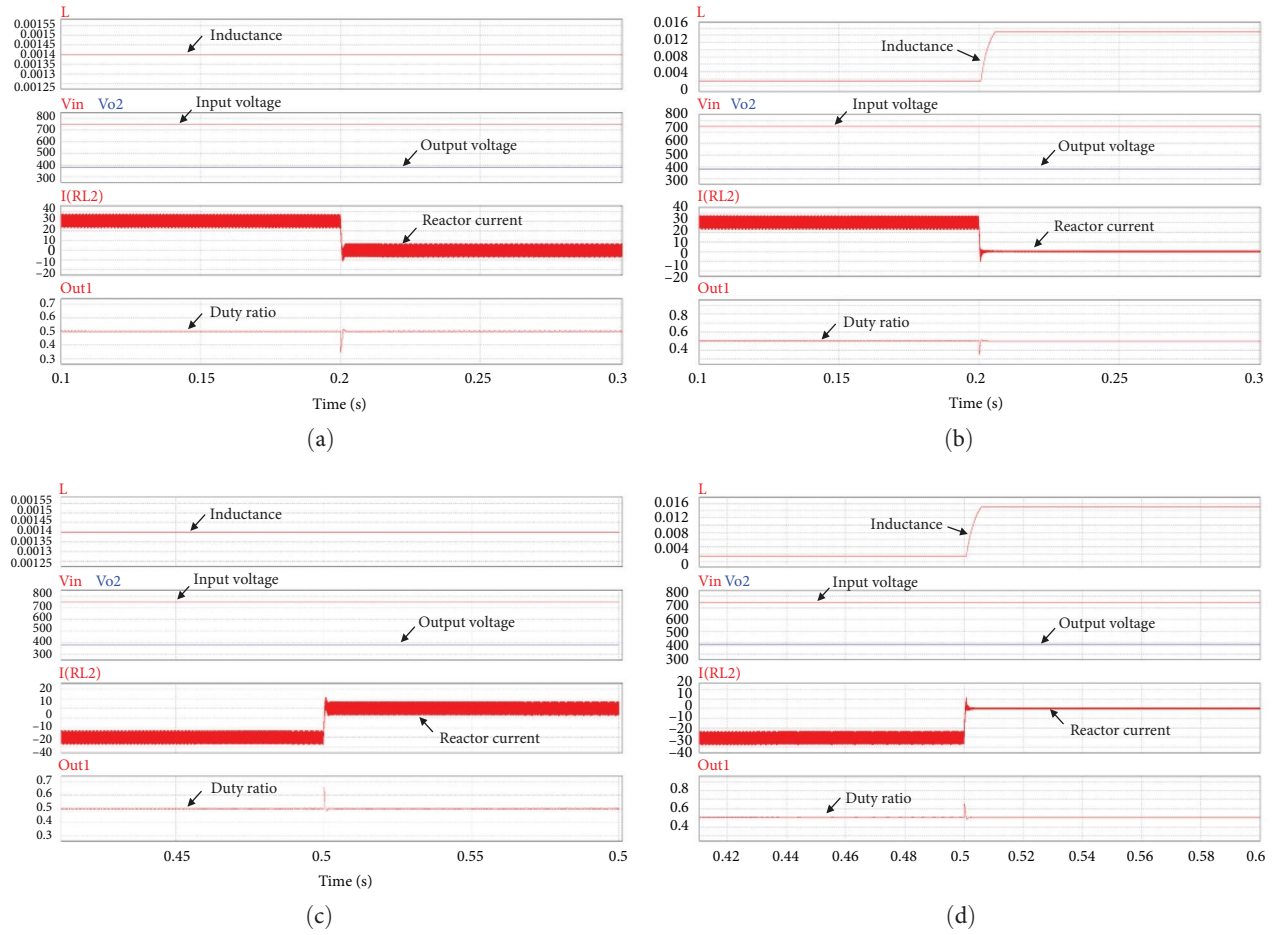

Figure 9: Reactor current characteristics according to the increase or decrease of the load current under current control of a bidirectional DC–DC converter; (a) when changing from 30 to 0 A with the fixed inductance, (b) from 30 to 0 A with the proposed variable inductance, (c) when changing from −30 to 0 A with the fixed inductance, and (d) when changing from −30 to 0 A with the proposed variable inductance.

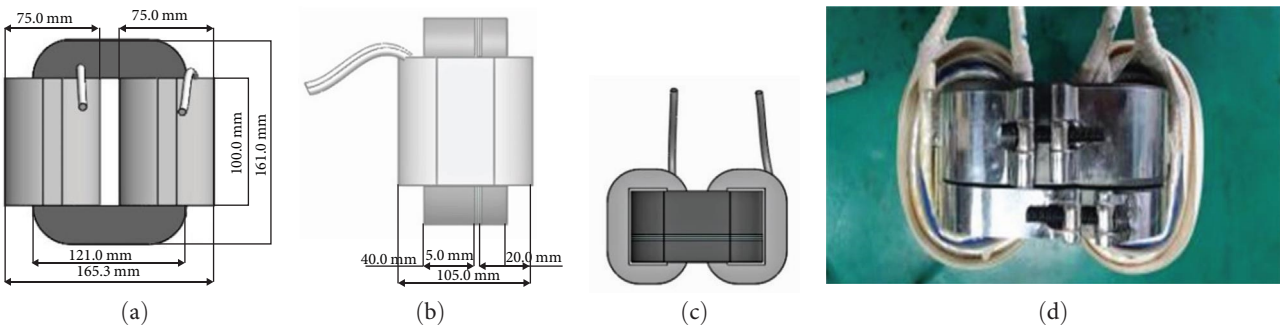

Figure 10: Case 1 reactor design: (a) front view, (b) side view, (c) top view, and (d) photo of a prototype.

cores is designed to be 1.5 times larger than the air gap of the large core. The critical parameters of the core used for the large and small reactors are given in Table 2, and the inductance of each reactor can be obtained from Equations (15) and (16)

$$L_m = \frac{\mu_r \mu_o A_c N^2}{l_c}, \tag{15}$$

$$L_a = \frac{\mu_o A_c N^2}{l_g}. \tag{16}$$

Since the bidirectional DC–DC converter using the proposed variable inductor operates in buck mode and boost mode, finding the optimal inductance value for both directions is difficult. Therefore, we need to calculate the inductance and select an appropriate core in the buck mode with

Table 2: Critical parameters of the magnetic component to implement Case 1 concept.

Core parameters	Large core (L_m) with large air gap		Small core (L_a) with small air gap		Air gap (L_m) (core-to-core)		Air gap (L_a) (core-to-core)		Unit
Permeability	μ_o	1.25664e-06	μ_o	1.25664e-06	μ_o	1.25664e-06	μ_o	1.25664e-06	H/m
	μ_r	400	μ_r	400	μ_r	1	μ_r	1	
Cross-sectional area	A_c	0.00124124	A_c	0.00062062	A_c	0.00124124	A_c	0.00062062	m^2
Windings	N	60	N	60	N	60	N	60	Turns
Length magnetic pass, air-gap	l_c	0.2079	l_c	0.2079	l_g	0.007	l_g	0.0001	m
Inductance	L_{cm}	10,805.3	L_{ca}	5,402.6	L_{gm}	802.2	L_{ga}	28,078.7	μH
	$2x$	21,610.6	$2x$	10,805.3	$2x$	1,604.5	$2x$	56,157.4	μH
Synthetic inductance		1,493.6		9,061.7		–		–	μH

the same power capacity and larger current. Considering the load power capacity, if the inductance of the primary inductor and auxiliary inductor at the allowable current peak is obtained using Equations (15) and (16), they are 1.5 and 9 mH, respectively, which is about 2.4 mH. Considering the output voltage of 380 V in buck mode under the condition of 24 kW load, the average inductor current is 65.8 A. Considering the switching frequency of 6 kHz and the voltage relationship from 750 to 380 V, the duty ratio of the switch is about 0.5. Therefore, the inductor's ripple current (peak-to-peak) is obtained as in Equation (17)

$$dI = V\left(\frac{dt}{L}\right) = (750 - 380)\frac{(0.5 \times 0.167 \times 10^{-3})}{2.4 \times 10^{-3}} = 12.87\text{A}. \tag{17}$$

Next, selecting a core that satisfies the calculated inductance and ripple current is necessary. Trade-off considering the size and price of the core, is common, but in this paper, a UU-Core made of Mn-Zn PC40 that satisfies the inductance and ripple current was selected. The number of turns of the inductor is determined as 60 Turns using Equation (18) in consideration of the A_L value of the core [50, 51].

$$N = \sqrt{\frac{L}{A_L}} = \sqrt{\frac{2.4\,mH}{667\,nH}} = 60\,\text{Turns}. \tag{18}$$

3.2.2. Design Procedure. There are several approaches to inductor design applied to power electronic systems. This paper implements variable inductance by combining a core with magnetic saturation and a core without magnetic saturation, slightly different from the general design method.

Step 1: in Case 1, the allowable ripple current of the inductor is first calculated by Equation (17), considering the load power capacity of the DC–DC converter. At this time, the current slope can be determined using the inductance value. This step determines an arbitrary inductance value by considering the current peak and slope (considering the current peak means considering the current rating of the switch that can be used).

Step 2: select a core (L_m) that can handle the allowable ripple current among the cores sold on the market. When selecting a core, it should be easily obtainable, and structurally, it should be considered whether two magnetic circuits can be composed of one MMF circuit like Case 1.

Step 3: as the auxiliary core (L_a) where magnetic saturation occurs, a core with the same magnetic permeability as L_m but with a smaller cross-section is selected.

Step 4: refer to the AL-value in the core data sheet and use Equation (18) to determine the number of windings. When a core is selected, the values in the data sheet are used for permeability and cross-sectional area depending on the core shape.

Step 5: since μ_r, μ_0, and A_c can be found through the core datasheet and the number of windings has been determined, adjust the air gap (l_c) in Equation (15) to obtain the desired L_m.

Step 6: adjust the air gap (l_g) in Equation (16) to obtain the desired L_a.

Step 7: if the desired inductance cannot be obtained even after adjusting the air gap, return to Step 1 and try again.

Cases 2 and 3 use the same procedure to design inductors.

Figure 11(a) is the analysis result using Flux3D for the current density flowing in the conductor. The current density of 6.5e + 06 A/m^2 is shown on the surface of the core, and the current density of about 4.817e + 06 A/m^2 appears on the curved surface where the wire is folded. Figure 11(b) shows the result of electromagnetic analysis. It shows 0.0123 Tesla in the primary core and 0.530 (tesla) in the auxiliary core.

3.2.3. Case 2: Single Magnetic Circuit in One MMF Circuit. Figure 12 shows a 3D view and prototype of a reactor applying the Case 2 concept. Case 2 uses three EE cores made of the same magnetic material. The key parameters are shown in Table 3. Design the air gap of the large core as 16 mm and the air gap of the small core as 1 mm. 70 Turns are wound using Litz wire 20SQ. The inductance of the large core (L_m) is 1.48 mH, and the inductance of the small core (L_a) is 33 mH.

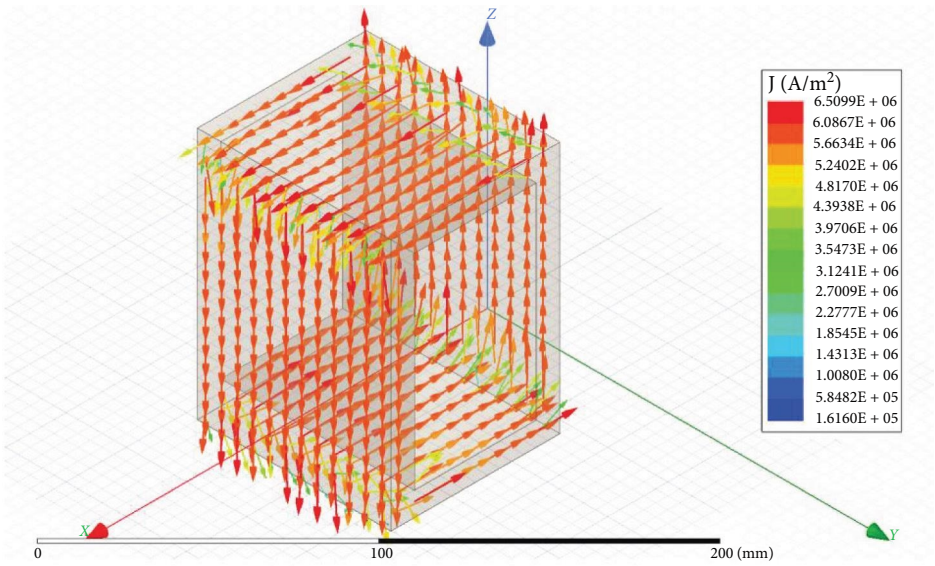

(a)

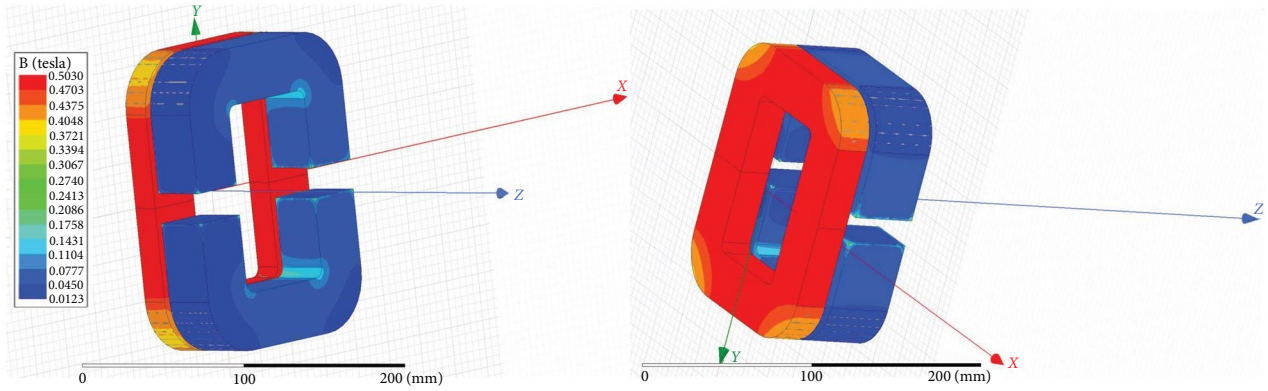

(b)

Figure 11: Current density and electromagnetic analysis for variable inductor case 1; (a) current density analysis and (b) electromagnetic analysis.

$$L = \frac{L_m \cdot L_a}{L_m + L_a}. \tag{19}$$

The combined inductance of Case 2 is calculated by Equation (19) because the primary inductor and auxiliary inductor are coupled in parallel. The ripple current is obtained using Equation (17) in the same way as Case 1, and a core that satisfies it is selected. In this paper, the Tangda EE160 core is selected. As in Equation (18), if the number of turns is calculated considering the A_L value of the core, it is 70 Turns.

Figure 13(a) is the analysis result using Flux3D for the current density flowing in the conductor. The current density of 1.866e + 05 A/m^{2}is shown on the surface of the core, and the current density of about 1.374e + 06 A/m^2 appears on the curved surface where the wire is folded. Figure 13(b) shows the result of electromagnetic analysis. It can be seen that the minimum value of 0.0028 Tesla appears in the air gap of the primary inductor core and the edge of each core, and the maximum value of 0.557 Tesla occurs in the air gap of the auxiliary inductor core.

3.2.4. Case 3: Magnetic Circuit by Two Magnetic Materials with Different Permeability in One MMF Circuit. Figure 14 shows the 3D view and prototype of the reactor to which the Case 3 concept was applied. Case 3 uses a toroidal core made of two different magnetic materials. Mega flux core with low permeability and EMI core with high permeability is used. The key parameters are listed in Table 4. Winding is 48 Turns using Litz wire 15SQ. As in the simulation, the inductance of the mega flux core is about 1.3 mH and the inductance of the EMI core is 12.8 mH.

$$L = \frac{\mu_r \mu_o C N^2}{2\pi} \ln\left(\frac{A}{B}\right), \tag{20}$$

$$B_m = \frac{\mu_r \mu_o \mathrm{NI}_{pk}}{l_c}. \tag{21}$$

The inductance of Case 3 is calculated by Equation (20) considering the cross-sectional area of the toroidal core, and

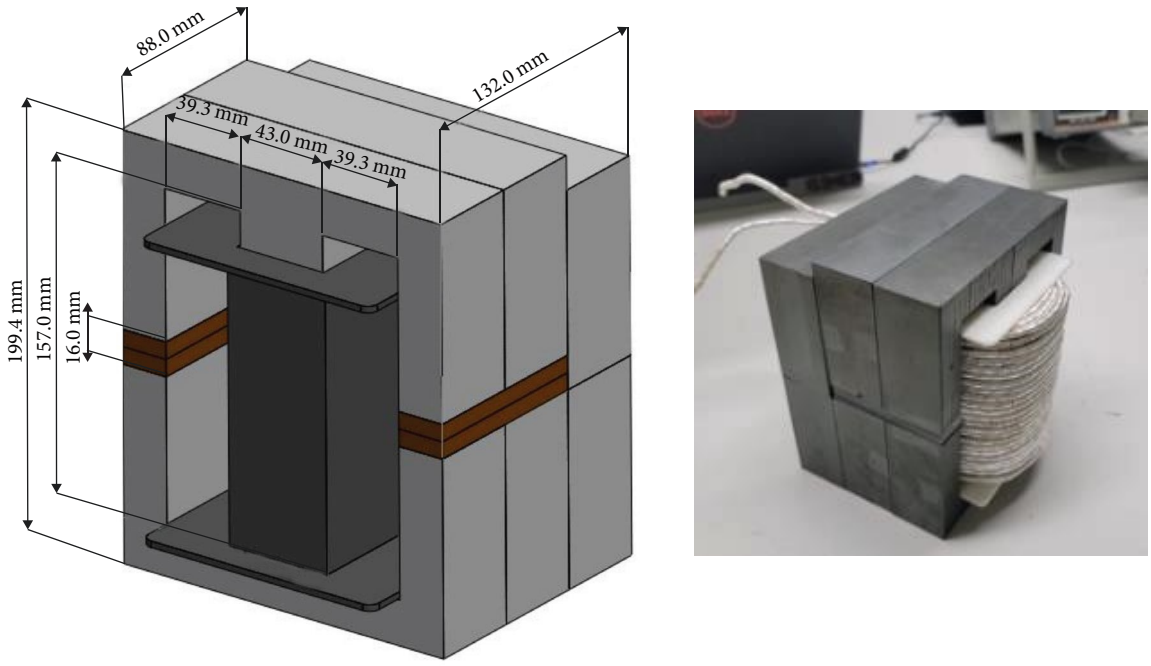

(a) (b)

Figure 12: Case 2 reactor design; (a) 3D view and (b) photo of a prototype.

Table 3: Critical parameters of the magnetic component to implement Case 2 concept.

Core parameters	Large core (L_m) with large air gap		Small core (L_a)		Air gap (core-to-core)		Unit
Permeability	μ_o	1.25664e-06	μ_o	1.25664e-06	μ_o	1.25664e-06	H/m
	μ_r	300	μ_r	300	μ_r	1	
Cross-sectional area	A_c	0.0010032	A_c	0.0010032	A_c	0.0010032	m^2
Windings	N	70	N	70	N	70	Turns
Length magnetic pass, air-gap	l_c	0.2082	l_c	0.2242	l_g	0.016	m
Inductance	L_{cm}	8,901.3	L_{ca}	8,265.7	L_{gm}	386.1	μH
	$4x$	35,605.3	$4x$	33,062.8	$4x$	1,544.3	μH
Synthetic inductance		1,480.1		33,062.8		–	μH

the magnetic flux density is defined by Equation (21). Using Equation (17), the ripple current is obtained in the same way as Case 1 and Case 2, and a core that satisfies this is selected. In this paper, Mega flux and EMI cores with different magnetic materials are selected. As in Equation (18), if the number of turns is calculated considering the A_L value of each core, it is 48 Turns.

Figure 15(a) is the analysis result using Flux3D for the current density flowing in the conductor. It can be seen that high-current density occurs on the core side of the auxiliary inductor. Figure 15(b) is the electromagnetic analysis result. It is as high as 0.4182 Tesla in the auxiliary inductor core and shows a value of 0.0866 Tesla in the core of the primary inductor.

3.3. Experimental Results. Figure 16 shows the experimental setup. The conventional reactor, three ways to implement the proposed variable reactors, and the bidirectional DC–DC converter are shown. To simulate the DC grid with two different voltages connected to both sides of the converter, a 750-V DC grid using a power supply and a 380-V DC grid using a battery cell are constructed. In addition, it consists of an oscilloscope (Wavesurfer 3024) for measuring the experimental waveform of the bidirectional converter, a power analyzer (WT1800) for measuring efficiency, and a PC for monitoring and control.

Figure 17 shows the reactor current waveform at no-load when the voltage across both ends of the bidirectional DC–DC converter is controlled to DC 750 V and DC 380 V. In the case of applying the conventional reactor in Figure 17(a), the current ripple is about 30 A. In Case 1, the reactor current ripple is about 20 A, the reactor with the small air gap core (L_a) is saturated, and the reactor with the large air gap core (L_m) operates. In Case 2 and Case 3, the reactor current ripple is about 1 A, and the current ripple is low due to the influence of the reactor with the small air gap core and the EMI core having a large inductance.

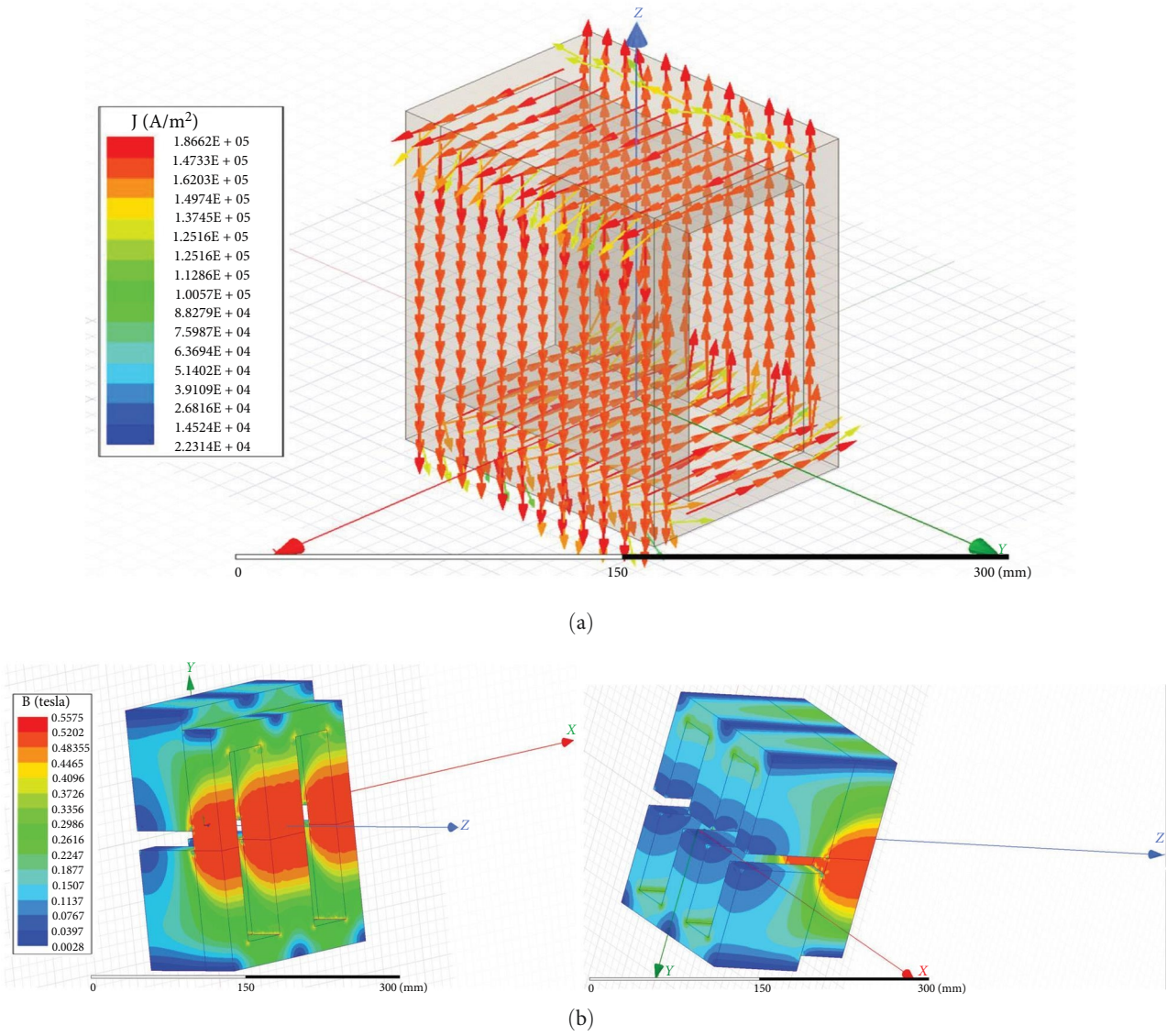

FIGURE 13: Current density and electromagnetic analysis for variable inductor Case 2: (a) current density analysis and (b) electromagnetic analysis.

Figure 18 is the experimental waveform of the reactor current ripple when the bidirectional DC–DC converter operates at 6 kW under voltage control. The conventional reactor in Figure 18(a) has a current ripple of about 30 A. Figure 18(b) shows the current ripple when the Case 1 reactor is applied. In Case 1, since the inductance of a large air gap core (L_m) is small and saturation occurs quickly, only up to 3 kW is tested. The current ripple appears to be about 30 A. Case 2 in Figure 18(c) has a current ripple of almost 24 A. In Case 3 of Figure 18(d), the current ripple appears according to the inductance of the large air gap core (L_m) due to the saturation of the small air gap core (L_a), measured at about 44 A.

Figure 19 shows the reactor current waveform during 12 kW operation under voltage control, with the voltages at both ends of the bidirectional DC–DC converter being DC 750 V and DC 380 V. In Figure 19(a), when the conventional reactor is applied, the current ripple is about 30 A and shows a constant value regardless of the load condition. In Case 1, the experiment is impossible because the main reactor is saturated at 12 kW operation. In Case 2, the reactor current ripple is about 24 A, and in Case 3, the current ripple is about 60 A. In Cases 2 and 3, the current ripple is determined according to the inductance of the large core as the small core is saturated.

Figure 20 is an experimental waveform to analyze the steady-state characteristics after no-load startup, assuming that the 750-V DC grid is connected to the 380-V DC grid. In Figure 20(b), the small core (L_a) of Case 1 is saturated, and the large core (L_m) is in operation. The initial soft-start

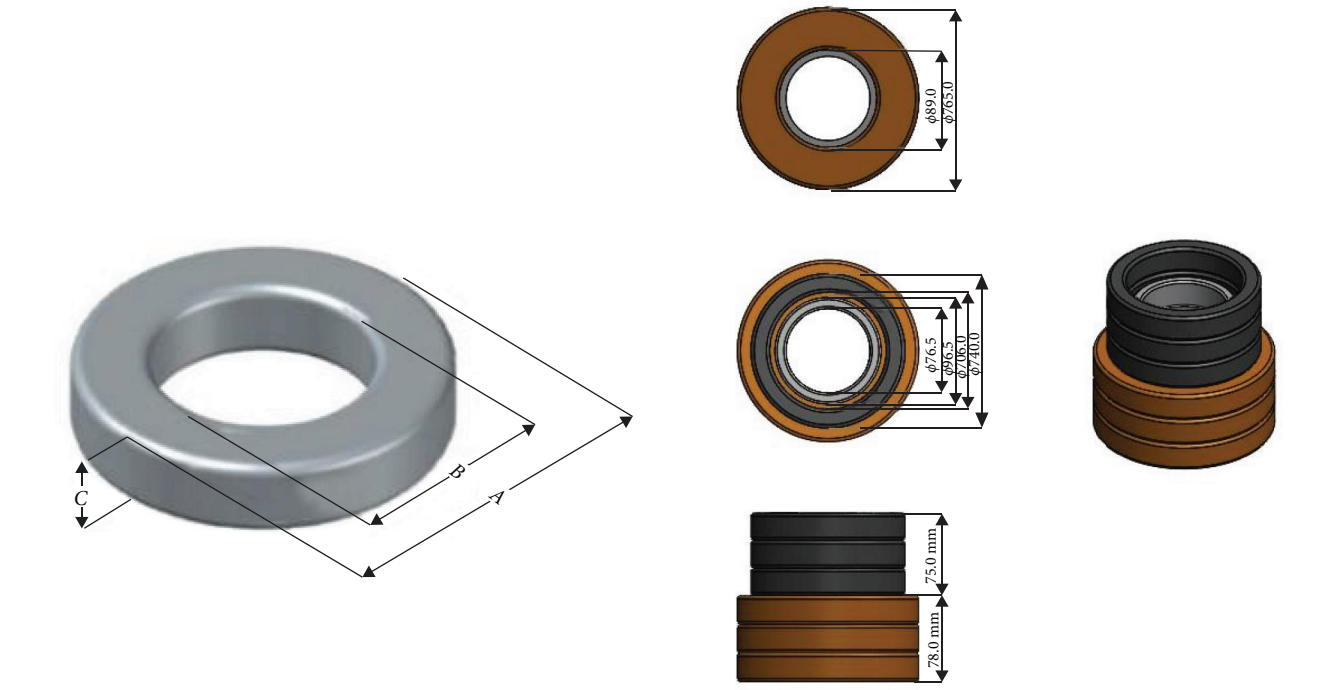

(a)

(b)

Figure 14: Case 3 reactor design: (a) 3D view and (b) photo of a prototype.

Table 4: Critical parameters of the magnetic component to implement Case 3 concept.

Core parameters	Mega flux (L_m)		EMI (L_a)		Unit
Permeability	μ_o	1.25664e-06	μ_o	1.25664e-06	H/m
	μ_r	60	μ_r	4,000	
Cross-sectional area	A	0.165	A	0.140	m
	B	0.089	B	0.106	m
	C	0.025	C	0.025	m
Windings	N	48	N	48	Turns
Inductance	L_{cm}	433.5	L_{ca}	12,819.6	μH
	$3x$	1,300.5	$1x$	12,819.6	μH
Total inductance		14,120.2			μH

response of the conventional and proposed reactors is the same. Still, the current ripple of the proposed reactor Cases 2 and 3 in the steady state is reduced to about 1/30.

Figure 21 is an experimental waveform to analyze the steady-state characteristics after starting with a 12 kW load when a 750-V DC grid is connected to a 380-V DC grid. In Figure 21(b), Case 1 shows the starting characteristics at 3 kW due to the saturation of the large air gap core (L_m). The initial attributes of the conventional and proposed reactor show similar characteristics even when the load is applied. In addition, it can be seen that the current ripple is identical to that of the conventional reactor because the small air gap core (L_a) of the proposed method is saturated in the 12 kW load operation. However, in Case 3, the inductance

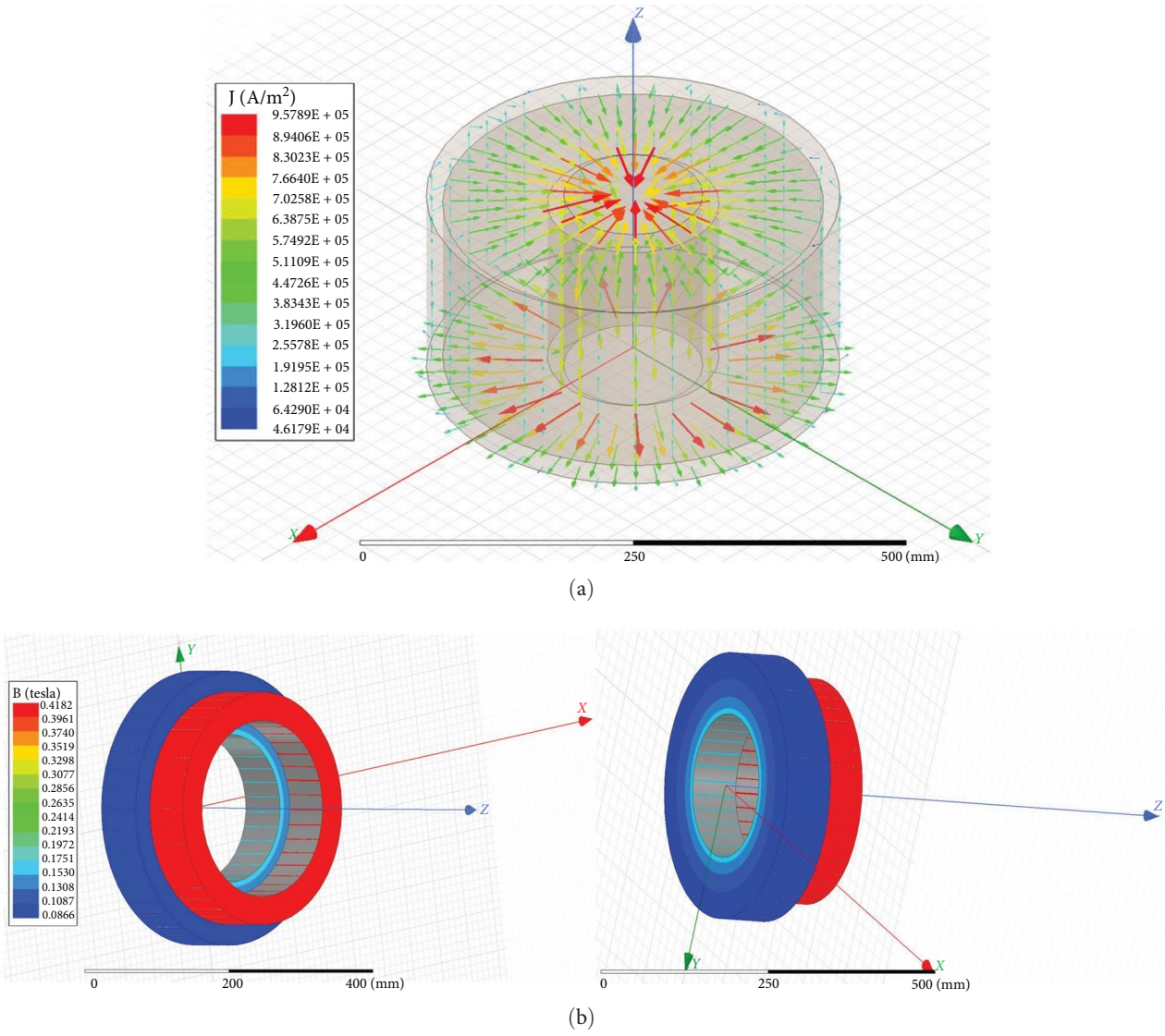

FIGURE 15: Current density and electromagnetic analysis for variable inductor case 3: (a) current density analysis and (b) electromagnetic analysis.

of the Mega flux core is small, about 1.3 mH, so the current ripple during load operation is enormous.

Figure 22 shows the experimental waveform in current control mode when the 750-V DC grid and 380-V DC grid are connected. The current ripple of the conventional reactor is about 30 A. The current ripple of the Case 1 reactor is about 20 A, the small air gap core (L_a) is saturated, and the large air gap core (L_m) is operating. The reactor current ripple in Cases 2 and 3 is about 1 A, and the current ripple is low due to the influence of the small air gap core (L_a) and the EMI core (L_a) having a large inductance.

Figure 23 is an experimental waveform transmitting 10 A from the 750-V DC grid to the 380-V DC grid under current control mode. The large air gap core (L_m) of Case 1 in Figure 23(b) shows saturation. The small air gap core (L_a) in Case 2 and the EMI core (L_a) in Case 3 is saturated, and the large air gap core (L_m) in Case 2 and the Mega flux core (L_m) in Case 3 are running. The current ripple of the conventional reactor is about 30 A. The current ripple of the Case 1 reactor is about 44 A, the current ripple of the Case 2 reactor is about 20 A, and the current ripple of the Case 3 reactor is about 36 A.

Figure 24 is an experimental waveform for transferring 20 A from a 750-V DC grid to a 380-V DC grid under current control mode. Case 1 cannot be tested due to saturation. In Case 2, the small air gap core (L_a) is saturated, and the large air gap core (L_m) is running. In Case 3, the EMI core (L_a) is saturated, and the Mega flux core (L_m) is operating. The current ripple of the conventional reactor shows about 30 A regardless of the load condition. The current ripple of the Case 2 reactor is about 24 A, and the current ripple of the Case 3 reactor is about 44 A.

Figure 25 is an experimental waveform for transferring 30 A from a 750-V DC grid to a 380-V DC grid with current control. Case 1 cannot be tested due to saturation. The small

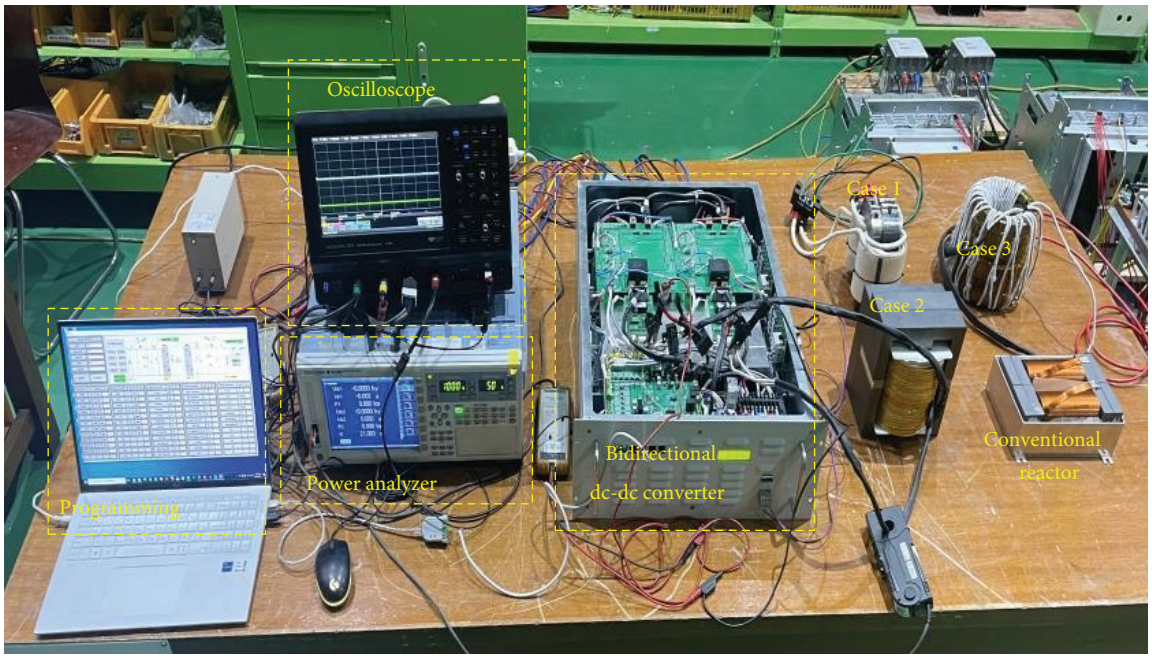

(a)

Power supply 1,500 V/±30 A

(b)

Battery 56 kWh, 1.2V 80 AH 590 cells

(c)

Figure 16: The experimental setup: (a) the existing reactor, the proposed three variable reactors, and the bidirectional DCDC converter for the experiment, (b) the power supply for the 750-V DC grid, and (c) the battery cell for the 380-V DC grid.

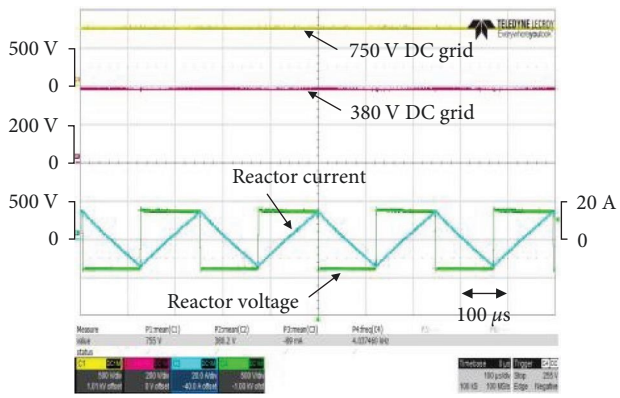

(a)

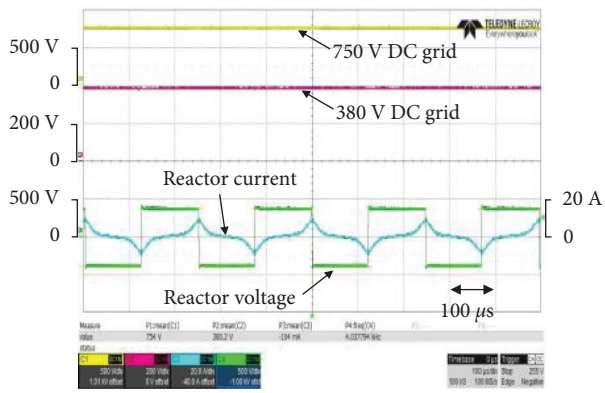

(b)

Figure 17: Continued.

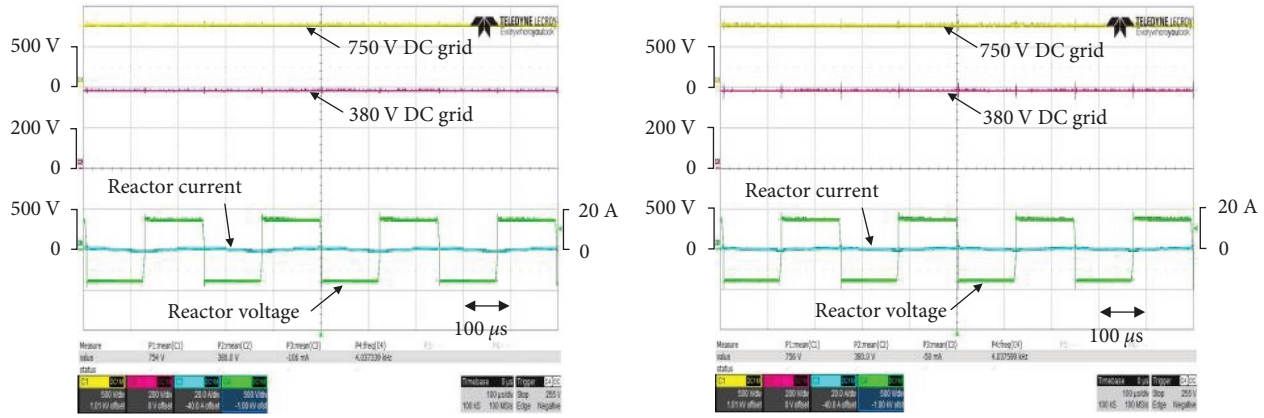

FIGURE 17: Reactor current ripple when the bidirectional DC–DC converter operates at no-load under voltage control; (a) conventional reactor, (b) Case 1, (c) Case 2, and (d) Case 3.

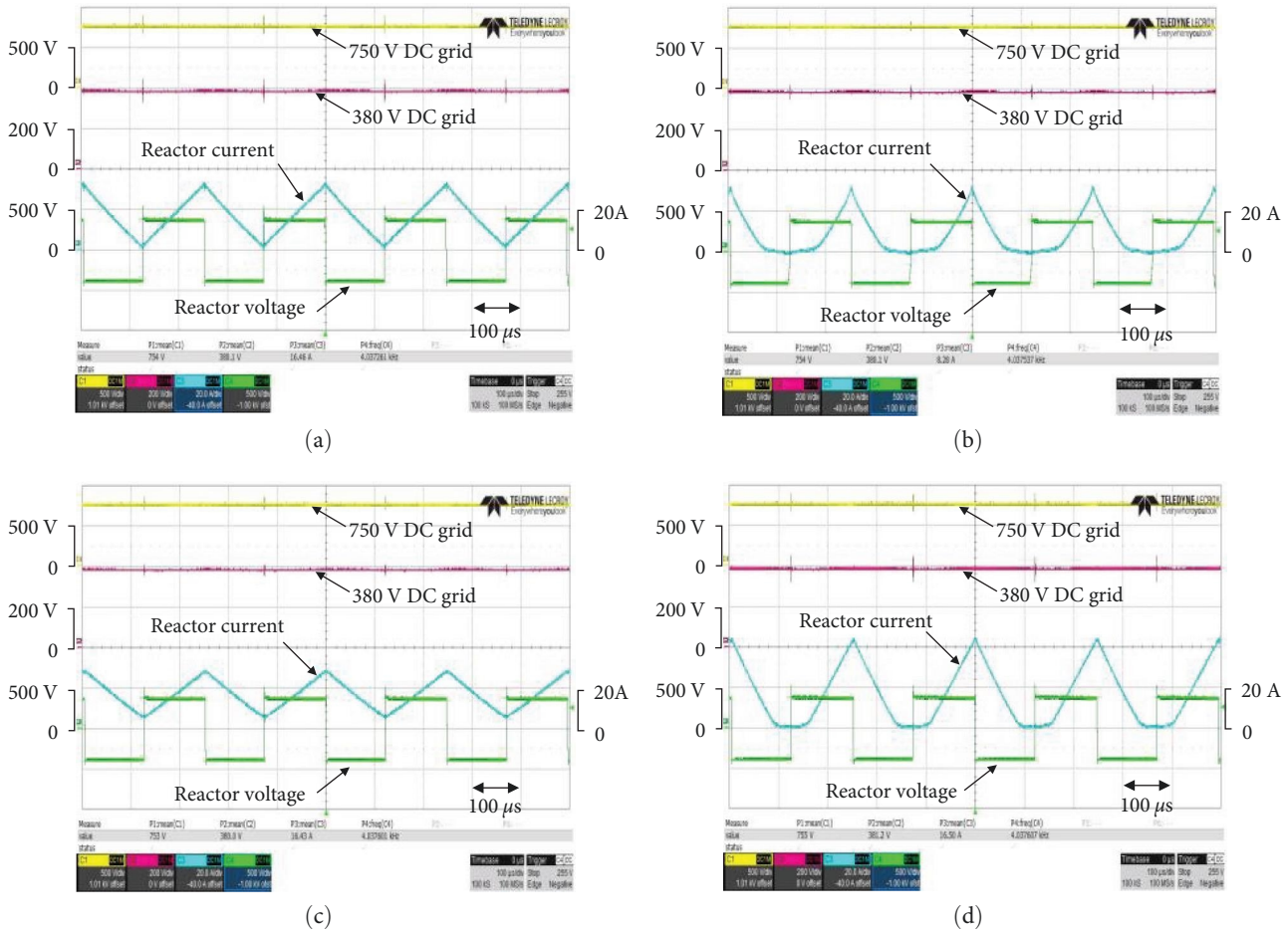

FIGURE 18: Reactor current ripple when the bidirectional DC–DC converter operates at 6 kW under voltage control,; (a) conventional reactor, (b) Case 1 @3 kW, (c) Case 2, and (d) Case 3.

air gap core (L_a) in Case 2 and the EMI core (L_a) in Case 3 is saturated, and the large air gap core (L_m) in Case 2 and the Mega flux core (L_m) in Case 3 are running. The current ripple of a conventional reactor represents about 30 A regardless of load conditions. The current ripple of the Case 2 reactor is about 24 A, and the current ripple of the Case 3 reactor is about 60 A.

Figure 26 is an experimental waveform in which the 750-V DC grid and the 380-V DC grid transfer 11 kW of power in both directions under current control mode. The

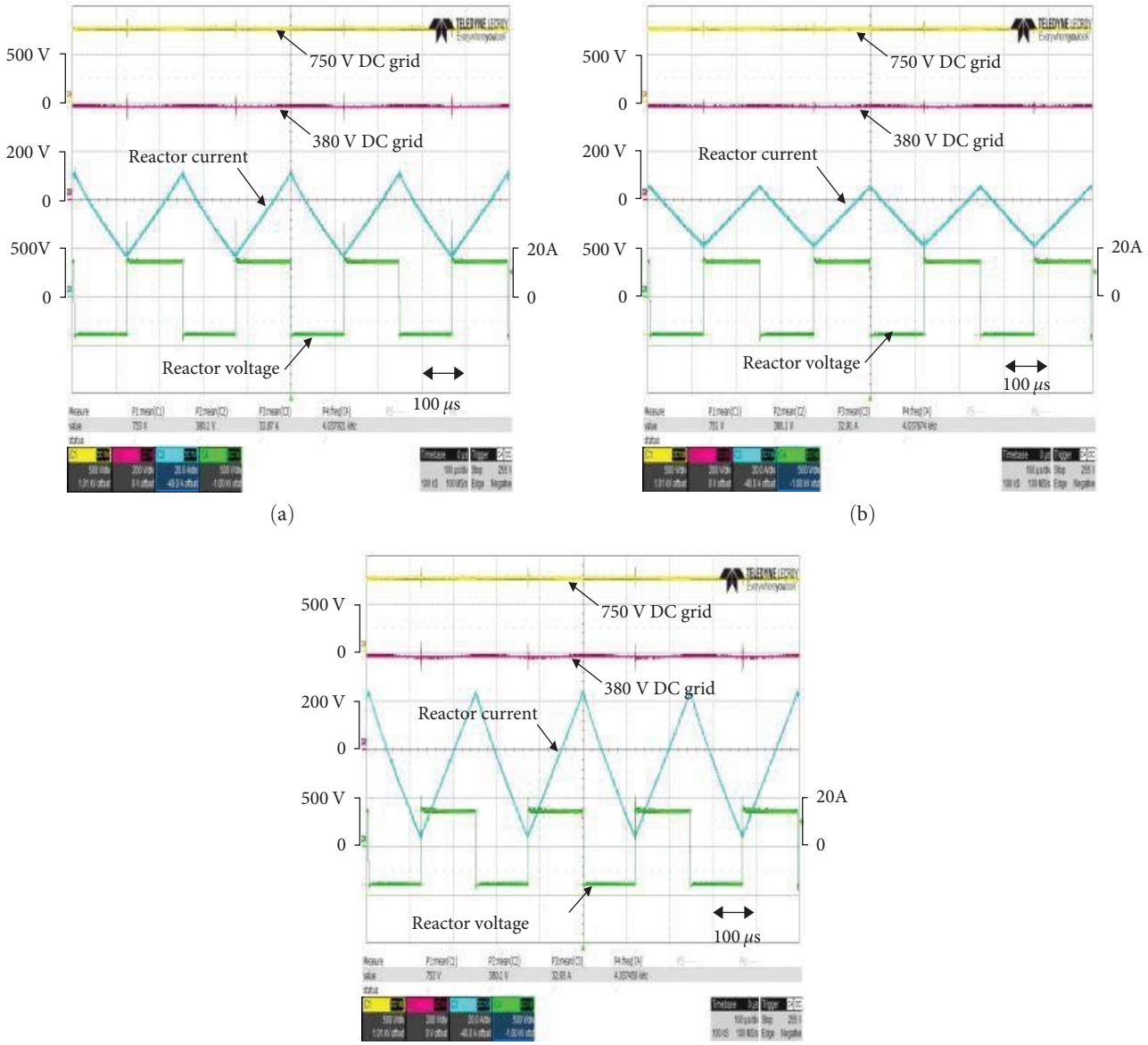

FIGURE 19: Reactor current ripple when the bidirectional DC–DC converter operates at 12 kW under voltage control, (a) conventional reactor, (b) Case 2, and (c) Case 3.

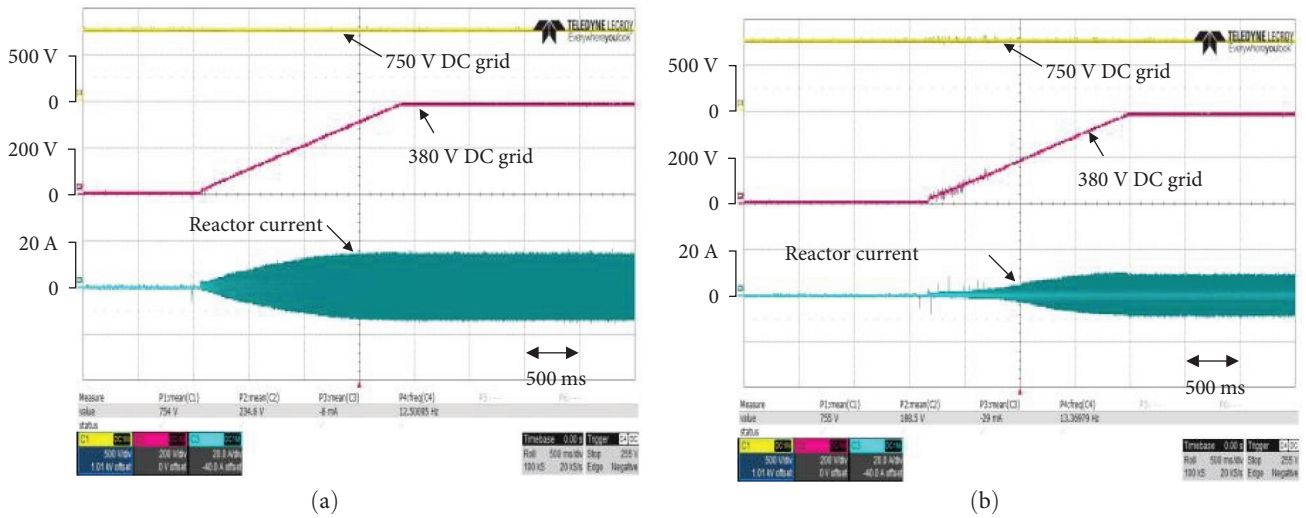

FIGURE 20: Continued.

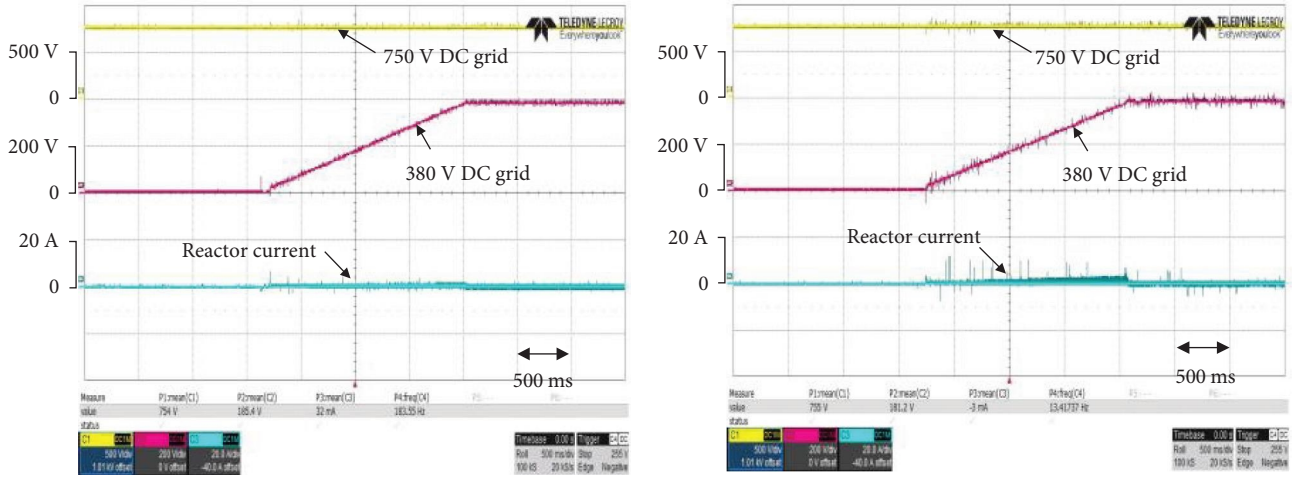

Figure 20: Experimental waveform to analyze the steady-state characteristics after no-load startup, assuming that the 750-V DC grid is connected to the 380-V DC grid; (a) conventional reactor, (b) Case 1, (c) Case 2, and (d) Case 3.

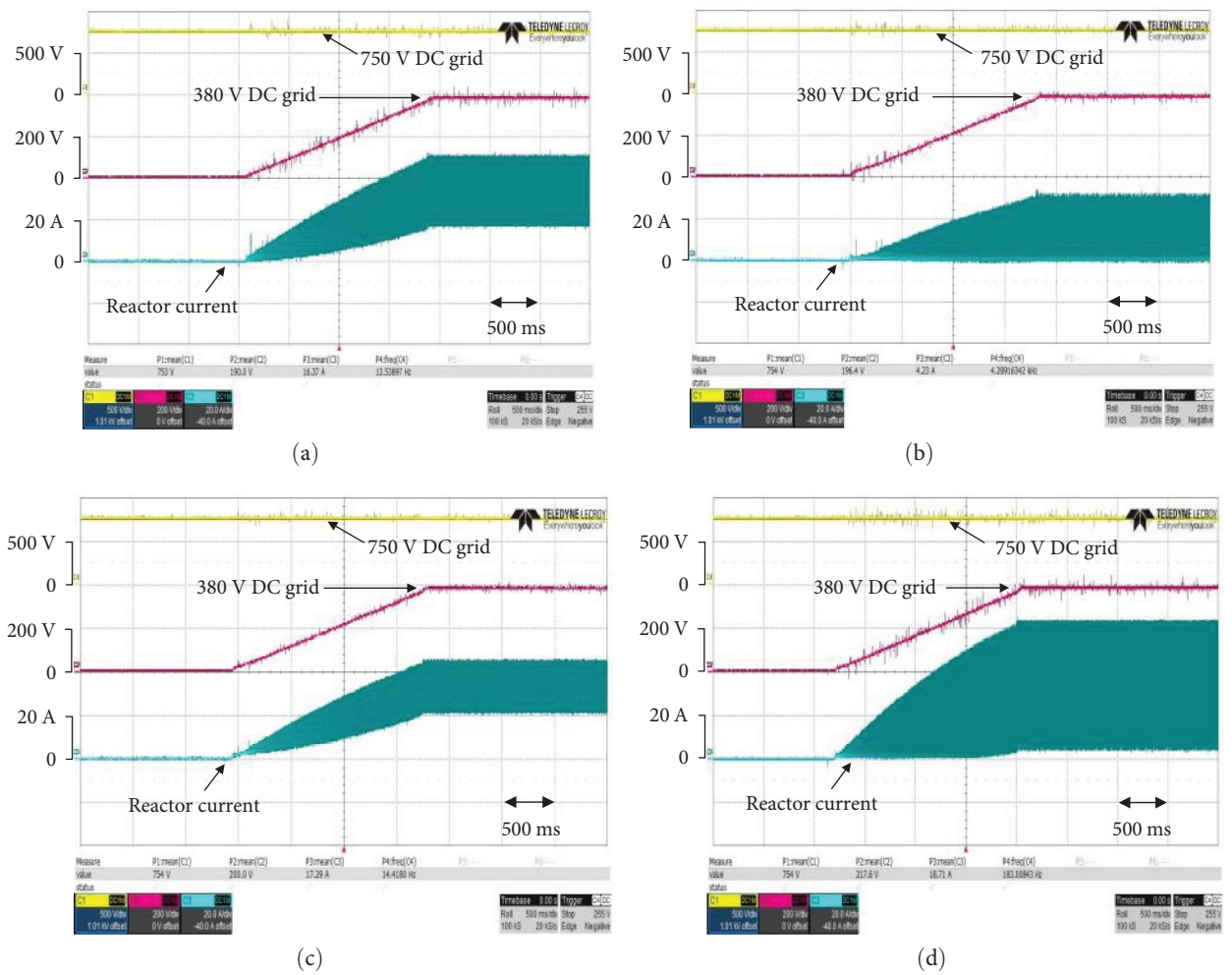

Figure 21: Experimental waveform to analyze the steady-state characteristics after starting a load of about 12 kW when a 750 V DC grid is connected to a 380 V DC grid: (a) conventional reactor, (b) Case 1 @3 kW, (c) Case 2, and (d) Case 3.

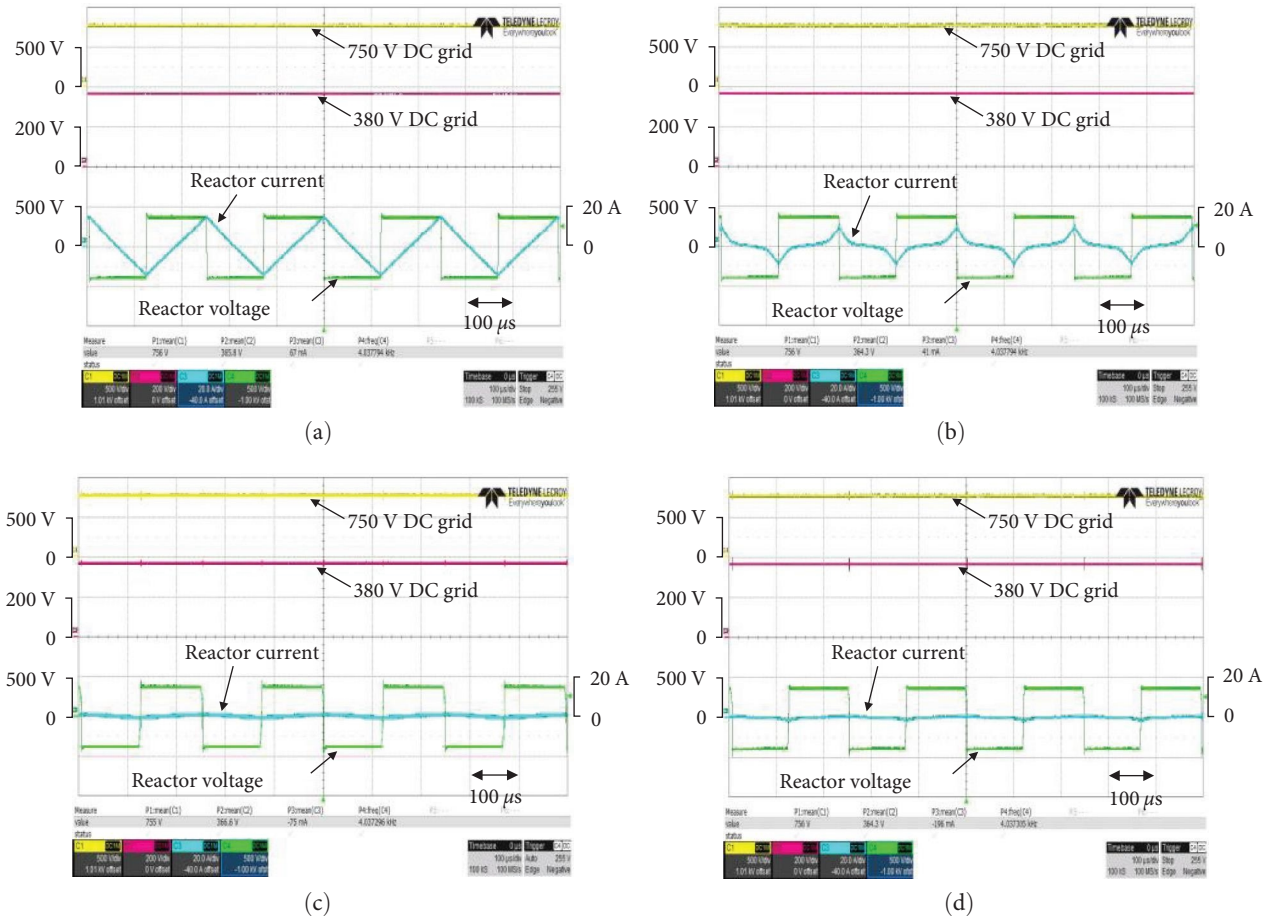

Figure 22: He experimental waveform at current control mode when the 750 V DC grid and 380 V DC grid are connected; (a) conventional reactor, (b) Case 1, (c) Case 2, and (d) Case 3.

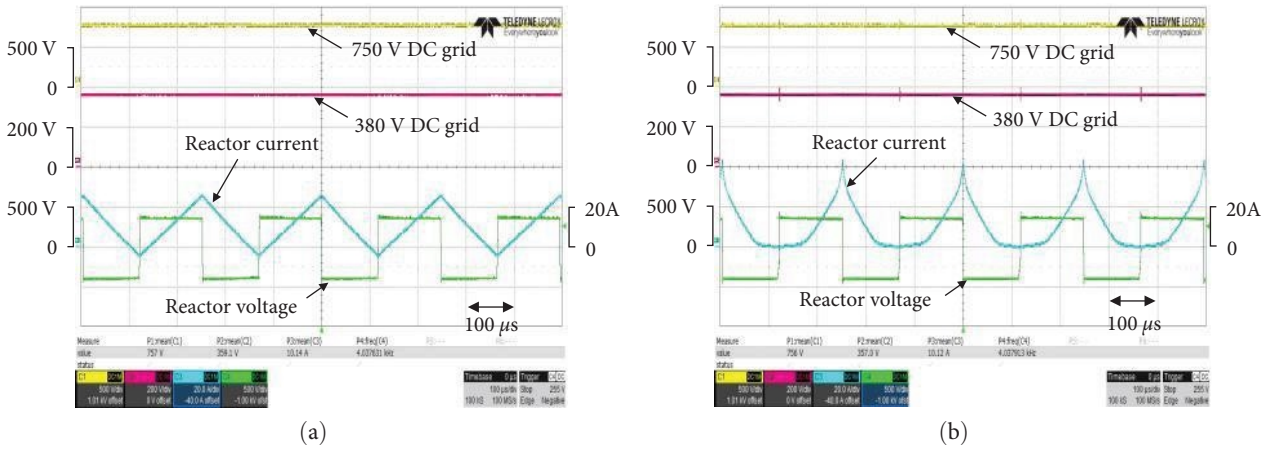

Figure 23: Continued.

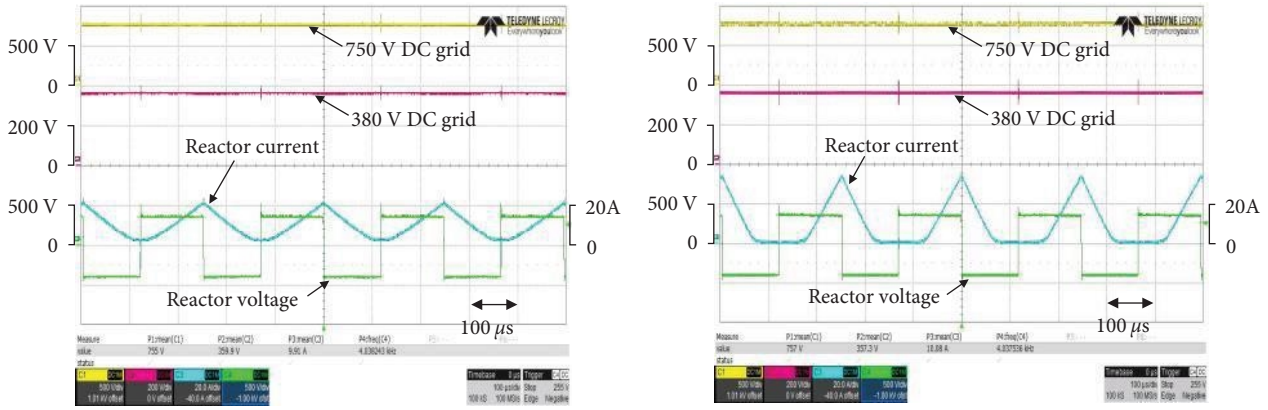

Figure 23: Experimental waveform transmitting 10 A from the 750 V DC grid to the 380 V DC grid under current control mode; (a) conventional reactor, (b) Case 1, (c) Case 2, and (d) Case 3.

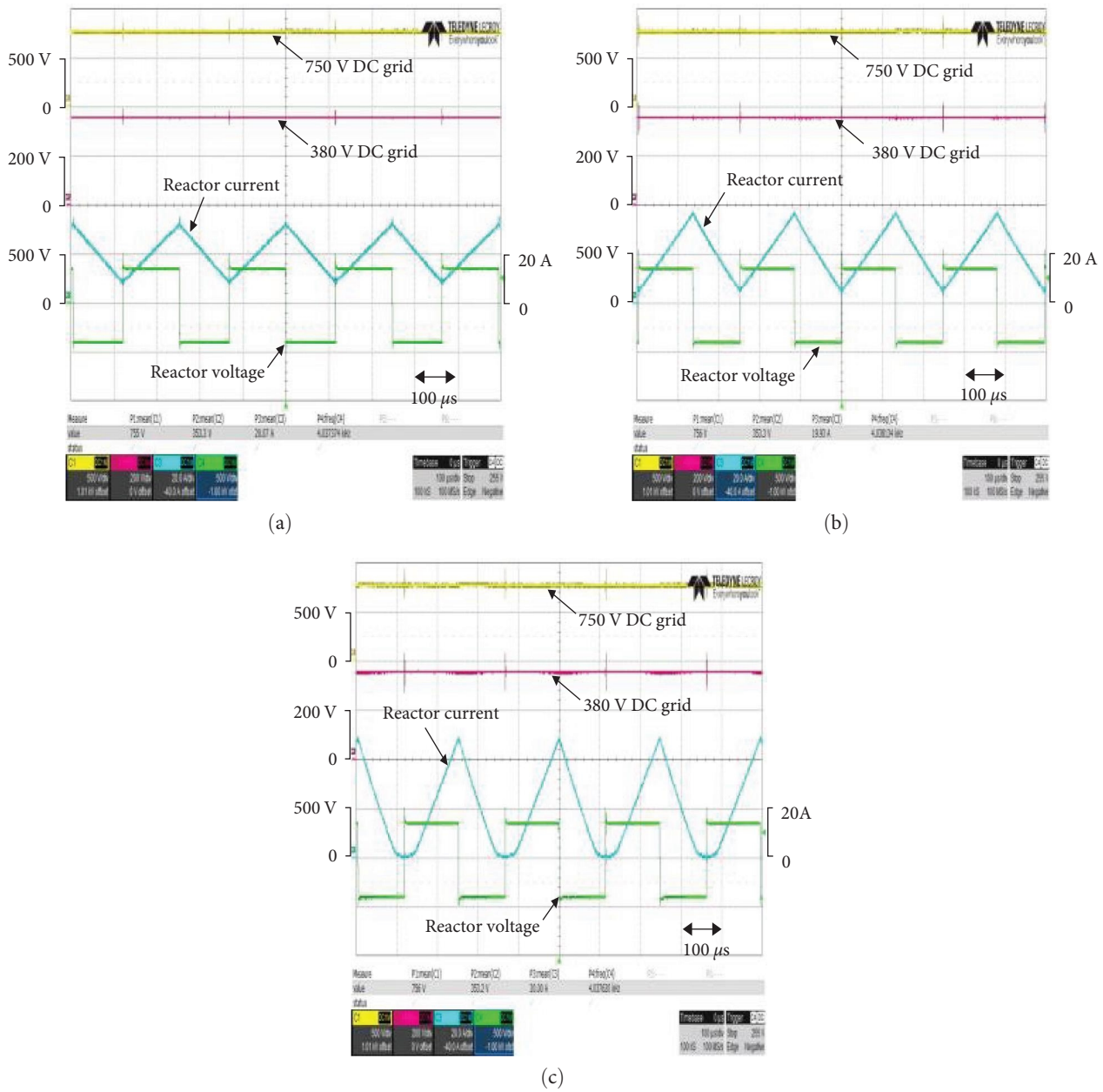

Figure 24: Experimental waveform transmitting 20 A from the 750 V DC grid to the 380 V DC grid under current control mode; (a) conventional reactor, (b) Case 2, and (c) Case 3.

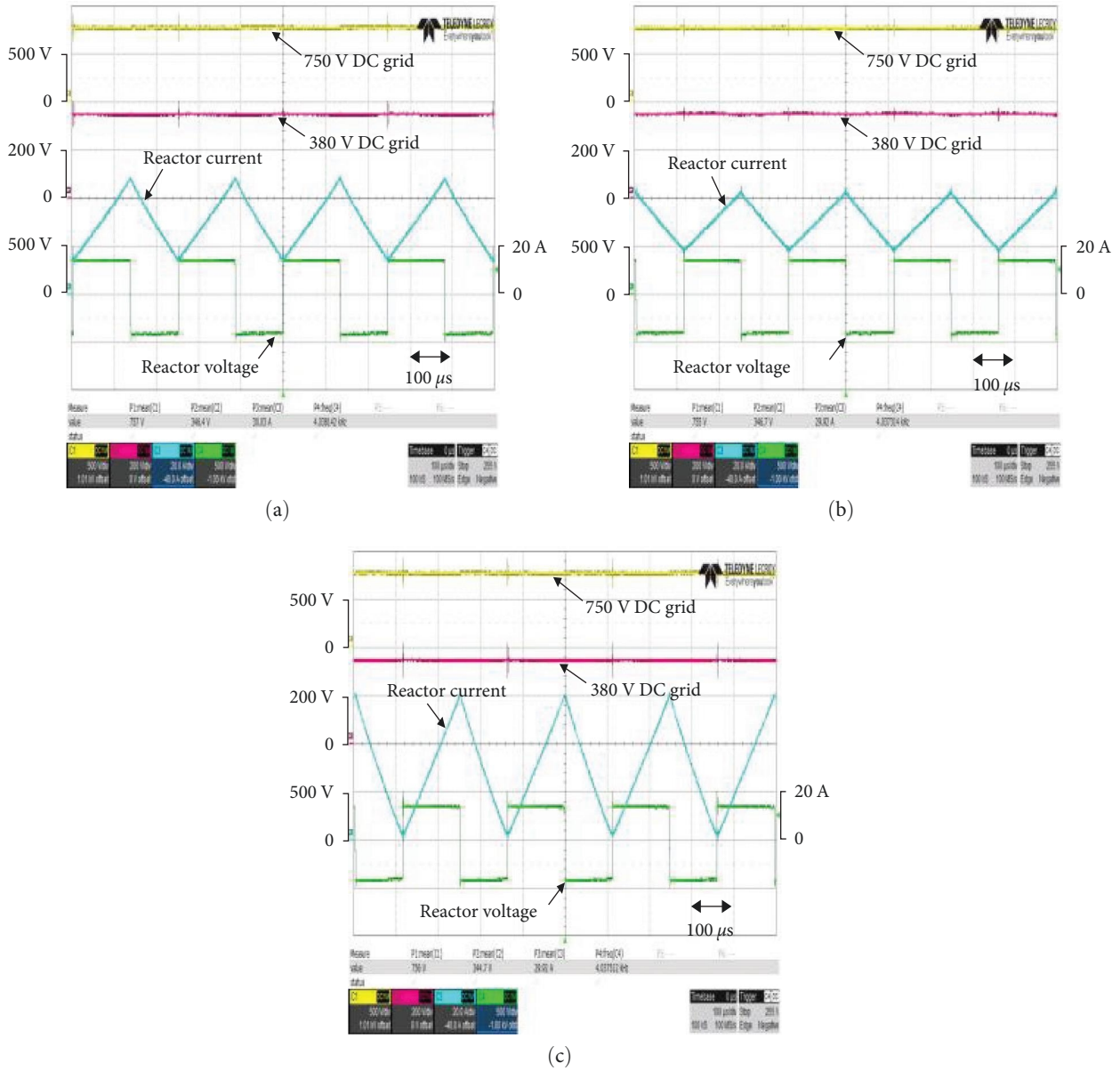

Figure 25: Experimental waveform transmitting 30 A from the 750 V DC grid to the 380 V DC grid under current control mode; (a) conventional reactor, (b) Case 2, and (c) Case 3.

conventional reactor in Figure 26(a) shows a constant current ripple even when the load changes. In the case of Case 1, the experiment is impossible due to the saturation of the reactor under the 11 kW load condition. In Cases 2 and 3, there is almost no current ripple.

Figure 27 analyzes the efficiency according to the load current in the bidirectional DC–DC converter. Cases 2 and 3 are more efficient at no-load than the converter using a conventional reactor. The loss of the converter at no load is 249.8 W in the conventional reactor. The converter using the Case 1 reactor is 152.3 W, the converter using the Case 2 reactor is 114.8 W, and the converter using the Case 3 reactor is 108.8 W. The converter loss at no load is the lowest in Case 3.

4. Conclusions

This paper's most important technical contribution is a method to reduce the current ripple at light load by designing the reactor of the bidirectional DC–DC converter to have variable inductance through magnetic saturation according to the load power capacity.

Cases 1 and 2 have large inductance due to the series connection of a small air gap core and a large air gap core under no-load or light-load conditions, thereby reducing current ripple. Since magnetic flux saturation occurs with the load current increase, it was confirmed that the inductance of the large air gap core operates only. Similarly, Case 3 maintains a large inductance by series coupling of the two

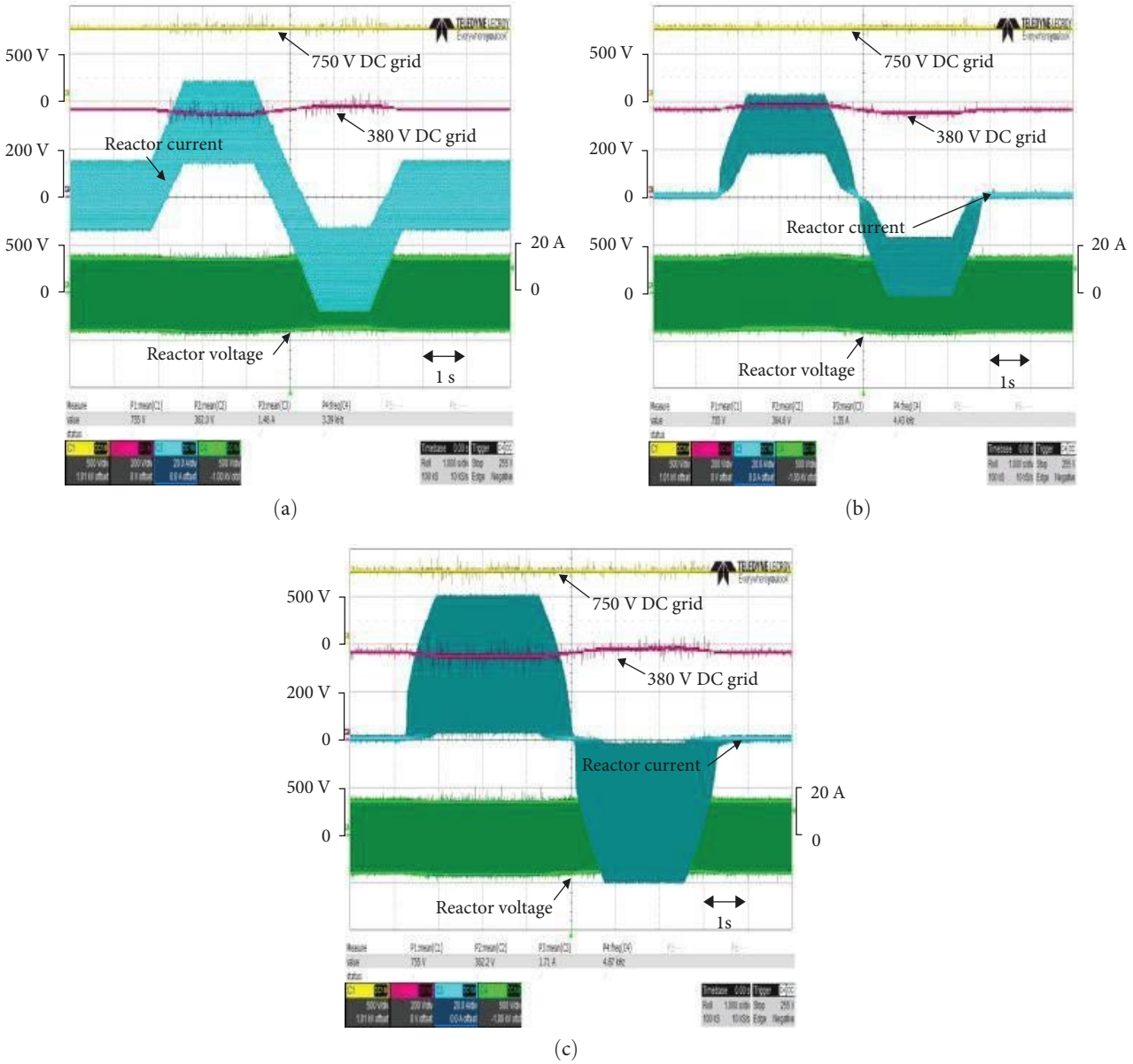

Figure 26: The experimental waveform in which the 750 V DC grid and the 380 V DC grid transfer 11 kW of power in both directions under current control mode: (a) conventional reactor, (b) Case 2, and (c) Case 3.

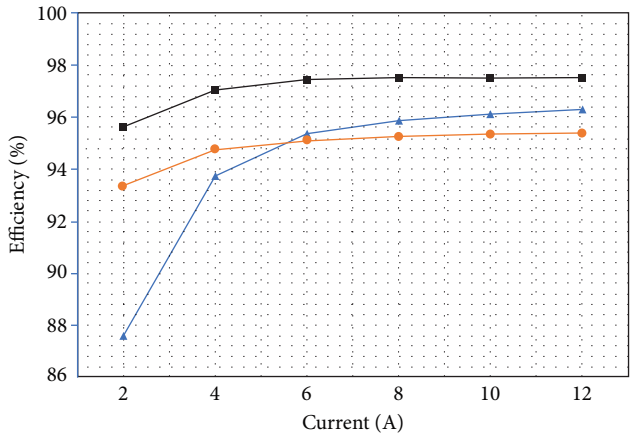

Figure 27: Bidirectional DC–DC converter power transfer efficiency according to the kinds of reactors.

cores under light load conditions. When the load current increases, the EMI core with high permeability saturates and operates as an inductance by the mega flux core, realizing variable inductance conditions according to the load current. As a result of the experiment, the proposed Case 3, at light load, showed an 8% efficiency improvement compared to the existing method, and the converter loss was a minimum of 108.8 W.

Suppose the proposed current ripple reduction technology using the variable reactor is applied to the DC distribution network of a microgrid. In that case, it is expected to increase the stability of the DC grid through harmonic reduction.

Data Availability

The data used to support the findings of this study are included within the article.

Conflicts of Interest

The authors declare that they have no conflicts of interest.

Acknowledgments

This research was financially supported by the Ministry of Small and Medium-Sized Enterprises (SMEs) and Startups (MSS), Korea, under the "Regional Specialized Industry Development Plus Program (R&D, S3365216)" supervised by the Korea Technology and Information Promotion Agency (TIPA) for SMEs.

References

[1] B. K. Bose, *Power Electronics in Renewable Energy Systems and Smart Grid*, Wiley, Hoboken, NJ, USA, 2019.

[2] O. C. Onar, J. Kobayashi, D. C. Erb, and A. Khaligh, "A bidirectional high-power-quality grid interface with a novel bidirectional noninverted buck–boost converter for PHEVs," *IEEE Transactions on Vehicular Technology*, vol. 61, no. 5, pp. 2018–2032, 2012.

[3] Y. Wang, X. Lin, and M. Pedram, "A near-optimal model-based control algorithm for households equipped with residential photovoltaic power generation and energy storage systems," *IEEE Transactions on Sustainable Energy*, vol. 7, no. 1, pp. 77–86, 2016.

[4] K. Jin, M. Yang, X. Ruan, and M. Xu, "Three-level bidirectional converter for fuel-cell/battery hybrid power system," *IEEE Transactions on Industrial Electronics*, vol. 57, no. 6, pp. 1976–1986, 2010.

[5] H. Heydari-doostabad and T. O'Donnell, "A wide-range high-voltage-gain bidirectional DC–DC converter for V2G and G2V hybrid EV charger," *IEEE Transactions on Industrial Electronics*, vol. 69, no. 5, pp. 4718–4729, 2022.

[6] A. Pannawan, T. Kaewchum, S. Somkun, and M. Hinkkanen, "Fast bus voltage control of single-phase grid-connected converter with unified harmonic mitigation," *IEEE Access*, vol. 11, pp. 6452–6466, 2023.

[7] M. Karimi-Ghartemani, S. A. Khajehoddin, P. Jain, and A. Bakhshai, "A systematic approach to DC-bus control design in single-phase grid-connected renewable converters," *IEEE Transactions on Power Electronics*, vol. 28, no. 7, pp. 3158–3166, 2013.

[8] N. Hou, P. Gunawardena, X. Wu, L. Ding, Y. Zhang, and Y. W. Li, "An input-oriented power sharing control scheme with fast-dynamic response for ISOP DAB DC–DC converter," *IEEE Transactions on Power Electronics*, vol. 37, no. 6, pp. 6501–6510, 2022.

[9] N. Hou and Y. W. Li, "Overview and comparison of modulation and control strategies for a nonresonant single-phase dual-active-bridge DC–DC converter," *IEEE Transactions on Power Electronics*, vol. 35, no. 3, pp. 3148–3172, 2020.

[10] F. Krismer and J. W. Kolar, "Efficiency-optimized high-current dual active bridge converter for automotive applications," *IEEE Transactions on Industrial Electronics*, vol. 59, no. 7, pp. 2745–2760, 2012.

[11] A. K. Tripathi, K. Mainali, D. C. Patel et al., "Design considerations of a 15-kV SiC IGBT-based medium-voltage high-frequency isolated DC–DC converter," *IEEE Transactions on Industry Applications*, vol. 51, no. 4, pp. 3284–3294, 2015.

[12] S. Poshtkouhi and O. Trescases, "Flyback mode for improved low-power efficiency in the dual-active-bridge converter for bidirectional PV microinverters with integrated storage," *IEEE Transactions on Industry Applications*, vol. 51, no. 4, pp. 3316–3324, 2015.

[13] H. Akagi, T. Yamagishi, N. M. L. Tan, S.-I. Kinouchi, Y. Miyazaki, and M. Koyama, "Power-loss breakdown of a 750-V 100-kW 20-kHz bidirectional isolated DC–DC converter using SiC-MOSFET/SBD dual modules," *IEEE Transactions on Industry Applications*, vol. 51, no. 1, pp. 420–428, 2015.

[14] A. R. R. Alonso, J. Sebastian, D. G. Lamar, M. M. Hernando, and A. Vazquez, "An overall study of a dual active bridge for bidirectional DC/DC conversion," in *2010 IEEE Energy Conversion Congress and Exposition*, pp. 1129–1135, IEEE, Atlanta, GA, USA, 2010.

[15] R. T. Naayagi, A. J. Forsyth, and R. Shuttleworth, "Bidirectional control of a dual active bridge DC–DC converter for aerospace applications," *IET Power Electronics*, vol. 5, no. 7, pp. 1104–1118, 2012.

[16] S.-J. Park, J. W. Park, K. H. Kim, and F.-S. Kang, "Battery energy storage system with interleaving structure of dual-active-bridge converter and non-isolated DC-to-DC converter with wide input and output voltage," *IEEE Access*, vol. 10, pp. 127205–127224, 2022.

[17] F. Calero, C. A. Cañizares, and K. Bhattacharya, "Dynamic modeling of battery energy storage and applications in transmission systems," *IEEE Transactions on Smart Grid*, vol. 12, no. 1, pp. 589–598, 2021.

[18] H. Bai and C. Mi, "Eliminate reactive power and increase system efficiency of isolated bidirectional dual-active-bridge DC–DC converters using novel dual-phase-shift control," *IEEE Transactions on Power Electronics*, vol. 23, no. 6, pp. 2905–2914, 2008.

[19] S. P. Engel, M. Stieneker, N. Soltau, S. Rabiee, H. Stagge, and R. W. De Doncker, "Comparison of the modular multilevel DC converter and the dual-active bridge converter for power conversion in HVDC and MVDC grids," *IEEE Transactions on Power Electronics*, vol. 30, no. 1, pp. 124–137, 2015.

[20] B. Zhao, Q. Song, J. Li, Y. Wang, and W. Liu, "Modular multilevel high-frequency-link DC transformer based on dual active phase-shift principle for medium-voltage DC power distribution application," *IEEE Transactions on Power Electronics*, vol. 32, no. 3, pp. 1779–1791, 2017.

[21] S. Inoue and H. Akagi, "A bidirectional DC–DC converter for an energy storage system with galvanic isolation," *IEEE Transactions on Power Electronics*, vol. 22, no. 6, pp. 2299–2306, 2007.

[22] A. Tanaka, E. Hiraki, and T. Tanaka, "A large-capacity capacitor simulator with a PWM rectifier and bi-directional DC-to-DC converter," in *2009 International Conference on Power Electronics and Drive Systems (PEDS)*, IEEE, Taipei, Taiwan, November 2009.

[23] M. Y. Chong, A. A. Rahman, N. A. Aziz, A. Khamis, and M. F. M. Basar, "Performance comparison of bidirectional converter designs for renewable power generation," in *2010 4th International Power Engineering and Optimization Conference (PEOCO)*, pp. 101–106, IEEE, Shah Alam, Malaysia, June 2010.

[24] Y. Sun, Y. Liu, M. Su, W. Xiong, and J. Yang, "Review of active power decoupling topologies in single-phase systems," *IEEE Transactions on Power Electronics*, vol. 31, no. 7, pp. 4778–4794, 2016.

[25] Y. Hu, W. Cao, S. J. Finney, W. Xiao, F. Zhang, and S. F. McLoone, "New modular structure DC–DC converter without electrolytic capacitors for renewable energy applications,"

IEEE Transactions on Sustainable Energy, vol. 5, no. 4, pp. 1184–1192, 2014.

[26] C. Liu and J.-S. Lai, "Low frequency current ripple reduction technique with active control in a fuel cell power system with inverter load," *IEEE Transactions on Power Electronics*, vol. 22, no. 4, pp. 1429–1436, 2007.

[27] H. Wen, W. Xiao, X. Wen, and P. Armstrong, "Analysis and evaluation of DC-link capacitors for high-power-density electric vehicle drive systems," *IEEE Transactions on Vehicular Technology*, vol. 61, no. 7, pp. 2950–2964, 2012.

[28] G. Liu, T. Caldognetto, P. Mattavelli, and P. Magnone, "Suppression of second-order harmonic current for droop-controlled distributed energy resource converters in DC microgrids," *IEEE Transactions on Industrial Electronics*, vol. 67, no. 1, pp. 358–368, 2020.

[29] M. Mellincovsky, V. Yuhimenko, Q.-C. Zhong, M. M. Peretz, and A. Kuperman, "Active DC link capacitance reduction in grid-connected power conversion systems by direct voltage regulation," *IEEE Access*, vol. 6, pp. 18163–18173, 2018.

[30] W. Cai, L. Jiang, B. Liu, S. Duan, and C. Zou, "A power decoupling method based on four-switch three-port DC/DC/AC converter in DC microgrid," *IEEE Transactions on Industry Applications*, vol. 51, no. 1, pp. 336–343, 2015.

[31] S. Li, G.-R. Zhu, S.-C. Tan, and S. Y. Hui, "Direct ac/dc rectifier with mitigated low-frequency ripple through inductor-current waveform control," *IEEE Transactions on Power Electronics*, vol. 30, no. 8, pp. 4336–4348, 2015.

[32] Y. Tang, W. Yao, P. C. Loh, and F. Blaabjerg, "Highly reliable transformerless photovoltaic inverters with leakage current and pulsating power elimination," *IEEE Transactions on Industrial Electronics*, vol. 63, no. 2, pp. 1016–1026, 2016.

[33] Q.-C. Zhong, W.-L. Ming, X. Cao, and M. Krstic, "Control of ripple eliminators to improve the power quality of DC systems and reduce the usage of electrolytic capacitors," *IEEE Access*, vol. 4, pp. 2177–2187, 2016.

[34] P. Strajnikov and A. Kuperman, "On the minimum DC link capacitance in practical PFC rectifiers considering THD requirements and load transients," *IEEE Transactions on Industrial Electronics*, vol. 69, no. 11, pp. 11067–11075, 2022.

[35] L. Gu, X. Ruan, M. Xu, and K. Yao, "Means of eliminating electrolytic capacitor in AC/DC power supplies for LED lightings," *IEEE Transactions on Power Electronics*, vol. 24, no. 5, pp. 1399–1408, 2009.

[36] D. G. Lamar, J. Sebastian, M. Arias, and A. Fernandez, "On the limit of the output capacitor reduction in power-factor correctors by distorting the line input current," *IEEE Transactions on Power Electronics*, vol. 27, no. 3, pp. 1168–1176, 2012.

[37] Y. Levron, S. Canaday, and R. W. Erickson, "Bus voltage control with zero distortion and high bandwidth for single-phase solar inverters," *IEEE Transactions on Power Electronics*, vol. 31, no. 1, pp. 258–269, 2016.

[38] S. Taghizadeh, M. Jahangir Hossain, J. Lu, and M. Karimi-Ghartemani, "An enhanced DC-bus voltage-control loop for single-phase grid-connected DC/AC converters," *IEEE Transactions on Power Electronics*, vol. 34, no. 6, pp. 5819–5829, 2019.

[39] R. Wang, F. Wang, D. Boroyevich et al., "A high power density single-phase PWM rectifier with active ripple energy storage," *IEEE Transactions on Power Electronics*, vol. 26, no. 5, pp. 1430–1443, 2011.

[40] P. T. Krein, R. S. Balog, and M. Mirjafari, "Minimum energy and capacitance requirements for single-phase inverters and rectifiers using a ripple port," *IEEE Transactions on Power Electronics*, vol. 27, no. 11, pp. 4690–4698, 2012.

[41] X. Cao, Q.-C. Zhong, and W.-L. Ming, "Ripple eliminator to smooth DC-bus voltage and reduce the total capacitance required," *IEEE Transactions on Industrial Electronics*, vol. 62, no. 4, pp. 2224–2235, 2015.

[42] Z. Qin, Y. Tang, P. C. Loh, and F. Blaabjerg, "Benchmark of AC and DC active power decoupling circuits for second-order harmonic mitigation in kilowatt-scale single-phase inverters," *IEEE Journal of Emerging and Selected Topics in Power Electronics*, vol. 4, no. 1, pp. 15–25, 2016.

[43] P. Vongkoon, P. Liutanakul, and N. Wiwatcharagoses, "Effective low-cost solution using cascaded connection of two modified notch filters to mitigate the second and third harmonic currents in single-phase dual-stage half-bridge microinverter," *IET Power Electronics*, vol. 12, no. 12, pp. 3118–3130, 2019.

[44] S. A. Khajehoddin, M. Karimi-Ghartemani, P. K. Jain, and A. Bakhshai, "DC-bus design and control for a single-phase grid-connected renewable converter with a small energy storage component," *IEEE Transactions on Power Electronics*, vol. 28, no. 7, pp. 3245–3254, 2013.

[45] H. Wang, H. S.-H. Chung, and W. Liu, "Use of a series voltage compensator for reduction of the DC-link capacitance in a capacitor-supported system," *IEEE Transactions on Power Electronics*, vol. 29, no. 3, pp. 1163–1175, 2014.

[46] W. Liu, K. Wang, H. S.-H. Chung, and S. T.-H. Chuang, "Modeling and design of series voltage compensator for reduction of DC-link capacitance in grid-tie solar inverter," *IEEE Transactions on Power Electronics*, vol. 30, no. 5, pp. 2534–2548, 2015.

[47] M. Merai, M. W. Naouar, I. Slama-Belkhodja, and E. Monmasson, "An adaptive PI controller design for DC-link voltage control of single-phase grid-connected converters," *IEEE Transactions on Industrial Electronics*, vol. 66, no. 8, pp. 6241–6249, 2019.

[48] S. Somkun and V. Chunkag, "Fast DC bus voltage control of single-phase PWM rectifiers using a ripple voltage estimator," in *IECON 2016 - 42nd Annual Conference of the IEEE Industrial Electronics Society*, pp. 2289–2294, IEEE, Florence, Italy, October 2016.

[49] K.-H. Kim, B.-C. Hwang, T.-V. Le, S.-M. Park, C.-H. Lee, and S.-J. Park, "Bi-directional converter system for light load by heterogeneous combined type reactor," *Electronics*, vol. 11, no. 18, Article ID 2924, 2022.

[50] R. Lenk, *Practical Design of Power Supplies*, McGraw-Hill, 1998.

[51] A. V. den Bossche and V. C. Valchev, *Inductors and Transformers for Power Electronics*, Taylor & Francis, 2005.